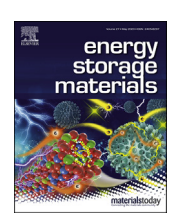
ELSEVIER

Contents lists available at ScienceDirect

# **Energy Storage Materials**

journal homepage: www.elsevier.com/locate/ensm



# Sulfur-nitrogen rich carbon as stable high capacity potassium ion battery anode: Performance and storage mechanisms



Lin Tao <sup>a</sup>, Yunpeng Yang <sup>a</sup>, Huanlei Wang <sup>a,\*\*</sup>, Yulong Zheng <sup>a</sup>, Hongchang Hao <sup>b</sup>, Wenping Song <sup>a</sup>, Jing Shi <sup>a</sup>, Minghua Huang <sup>a</sup>, David Mitlin <sup>b,\*</sup>

- <sup>a</sup> School of Materials Science and Engineering, Ocean University of China, Qingdao, 266100, People's Republic of China
- b Walker Department of Mechanical Engineering, The University of Texas at Austin, Austin, TX, 78712-1591, USA

#### ARTICLE INFO

Keywords:
Potassium metal battery (PMB)
Potassium ion battery (PIB,KIB)
Graphene
Carbon nanosheet
Solid electrolyte interphase (SEI)

#### ABSTRACT

Combined sulfur and nitrogen (S=12.9 at.%, N=9.9 at.%) rich carbons are synthesized for potassium ion anode applications. The low-surface-area carbons ( $56~m^2~g^{-1}$ ) have sulfur covalently bonded to the structure, with minimum unbound "free" sulfur. This allows for exceptional rate capability and stability: Capacities of 437, 234 and 72 mAh  $g^{-1}$  are achieved at 0.1, 1 and 10 A  $g^{-1}$ , with 75% retention at 2 A  $g^{-1}$  after 3000 cycles. These are among the most favorable capacity-cyclability combinations reported in potassium ion battery carbon literature. As a proof of principle, the carbons are incorporated into a potassium ion capacitor with state-of-the-art energy and power (e.g. 110 W h kg<sup>-1</sup> at 244 W kg<sup>-1</sup>). According to XPS analysis, the reaction of nitrogen with K<sup>+</sup> is distinct from that of K<sup>+</sup> with sulfur. The N and N–O moieties undergo a series of complex multi-voltage reactions that result in both reversible and irreversible changes to their structure. The K–S reactions involve a combination of reversible adsorption and reversible formation of sulfides, thiosulfate and sulfate. GITT and EIS analysis indicate that incorporation of S into the N-rich carbon increases the K<sup>+</sup> solid-state diffusion coefficient by factors ranging from ~3 to 8, depending on the voltage. The diffusivities are asymmetric with charging  $\nu$ s. discharging, signifying distinct reaction pathways. The covalently bound sulfur also has a positive influence on the solid electrolyte interphase (SEI) formation, at early and at prolonged cycling.

### 1. Introduction

Large-scale energy storage systems play a key role in advancing smart power grid and other stationary and municipal renewable energy storage applications [1–7]. Lithium-ion batteries (LIBs) may become restricted for such large-scale application due to limited supply of Li precursors and of Co used in most LIB cathodes [8–11]. Owing to the abundance and low cost of potassium precursors, potassium ion batteries (PIBs, KIBs) are becoming considered as one potential alternative to LIBs for applications where absolute "best" performance is not essential [12–20]. However, many well-established anode materials in LIBs are poorly suitable for KIBs. One example is graphite, which performs badly with potassium due to the larger ionic size of K $^+$  (1.38 Å) relative to Li $^+$  (0.76 Å), and a difference in the ion-carbon bonding [21,22]. The potassium ion will cause too large of volume expansion during charging, leading to low capacity especially at higher charge rates, as well as poor cyclability. However, with electrode materials tuned specifically for hosting K $^+$ 

rather than  ${\rm Li}^+$ , KIBs may be promising in their performance. Potassium ions possess advantages in terms of transport in the electrolyte. The weaker Lewis acidity of K<sup>+</sup> versus  ${\rm Li}^+$  results in a lower Stoke's radius of solvated ions, a higher transport number and higher mobility [23]. The challenge is in the solid-state, where the larger K ions are naturally slower diffusers in most materials.

To date, various anode materials have been investigated for KIBs, including carbons [24–28], alloys [16,29], metal compounds (oxide [30–32], sulfide [33,34], phosphide [35,36], selenide [37,38], MXenes [39]), organic compounds [40,41], etc. Among them, carbonaceous materials are receiving perhaps the most interest, owing to their high electrical conductivity, low cost and wide availability [42,43]. This includes carbons with a range of morphologies and structures, including porous carbons [44], carbon microspheres [45,46], and carbon nanotubes [47]. Heteroatom doping can modulate the chemical and electronic environment, thus improving a range of electrochemical properties [48, 49]. For example, nitrogen dopants have been extensively adopted in

E-mail addresses: huanleiwang@gmail.com (H. Wang), David.Mitlin@austin.utexas.edu (D. Mitlin).

 $<sup>^{\</sup>ast}$  Corresponding author.

<sup>\*\*</sup> Corresponding author.

carbons, because they can enhance the electronic conductivity of carbon, introduce more active sites and defects in carbon frameworks, as well as improve reaction activity [49–51]. Heteroatom-rich carbons, for example containing B, N, S and P, have been shown to generally possess higher reversible capacities than their undoped counterparts [48–53]. A range of heteroatom doping strategies are widely employed to boost the reversible capacities and often the rate capabilities of Li and Na ion battery anodes [54–57]. From that vantage, K specific carbons are less mature, although there are impressive results concerning O and N doping [49,58–60].

Sulfur heteroatoms will provide additional reversible storage capacity by reversible reactions with K, Na and Li [61,62]. However, unlike Na and Li where more literature is available, S-rich carbons for K are in the early stages of scientific inquiry. Mai's group firstly reported S-doped graphene as anodes for PIBs and highlighted the reaction mechanism for K-ion storage [63]. Ding et al. has reported sulfur-grafted hollow carbon spheres for KIB anodes, exhibiting a high reversible capacity of 581 mAh  $g^{-1}$  at 25 mA  $g^{-1}$  [64]. Yang' group recently reported 3D sulfur and nitrogen codoped carbon nanofiber aerogels used for PIBs, exhibiting a capacity of 356 mAh g<sup>-1</sup> at 100 mA g<sup>-1</sup> [65]. Dual doped carbons appear to synergize the effect of each specie in boosting the reversible capacity of the carbon. Recently published reports for dual doped carbon anodes include N/O dual-doped hard carbon [66], S/O co-doped porous hard carbon microspheres [45], and P/N co-doped carbon [50,67-68], all of which deliver promising electrochemical properties. Although S and N co-doping has been employed successfully in carbons for enhanced Na storage [69-72], it is much less common for K applications [73].

In this study, we synthesize a S-doped N-rich carbon by carbonizing a poly (acrylamide-co-acrylic acid) potassium salt-sulfur precursor. Taking advantage of its water adsorption propensity, elemental sulfur is introduced into the polymer salt through a reaction between sodium thiosulfate and dilute hydrochloride acid. The resultant carbon contains uniquely large content of S (12.9 at.%) and N (9.9 at.%), and thereby demonstrate exceptional reversible K storage capacity, superior rate performance, as well as excellent cycling stability. In parallel, we explore the fundamental aspects of potassiation - depotassiation reactions in these materials, thereby providing new mechanistic insight.

# 2. Materials and methods

# 2.1. Material preparation

In a typical synthesis process for Sulfur doped N-rich Carbon (S-NC), 7.75g sodium thiosulfate (Na<sub>2</sub>S<sub>2</sub>O<sub>3</sub>) was fully dissolved into 30ml deionized water. Subsequently 1g poly (acrylamide-co-acrylic acid) potassium salt was added slowly into the solution to form a hydrogel. This process was performed at room temperature. The dilute hydrochloride acid (3 M, 20mL) was slowly added drop by drop, with the hydrogel immediately turning yellow. After stirring for 1 h, the obtained yellow hydrogel was frozen and then freeze-dried for 72 h. The resultant yellow precursor was sealed in an alumina boat and heated inside a tubular furnace under a N2 atmosphere at 280 °C for 1 h, followed by carbonization at 800 °C for 2 h. Finally, the produced carbon powder was then washed in dilute hydrochloric acid and deionized water to remove the inorganic impurities and dried at 80 °C for 12 h. As a baseline, N-rich Carbon (NC) was synthesized by the similar procedure but without the addition of Na<sub>2</sub>S<sub>2</sub>O<sub>3</sub> and HCl. All the reagents were employed in their as received condition, without further purification.

#### 2.2. Materials characterization

The morphology of S-NC and NC was examined by scanning electron microscopy (SEM), using a Hitachi S4800 operated at 15kV. The structure of the carbons was analyzed by transmission electron microscopy (TEM), employing a JEOL 2010F operated at 200 kV. X-ray diffraction (XRD) was carried using a Bruker D8 Advance powder diffractometer,

with Cu K $\alpha$  radiation. The Raman spectra measurements were performed using a Lab RAM HR800, with an effective laser power on the sample of 5 mW, an excitation laser wavelength of 532 nm, and a spot size of 1 mm. The specific surface area and pore size distribution of the carbons was obtained using a Micromeritics TriStar II 3020 surface characterization analyzer. X-ray photoelectron spectroscopy (XPS) analysis was performed using a Thermo ESCALAB 250XI. The carbon's electrical conductivity was measured using a multifunction digital four-probe tester (ST2253). Thermogravimetric (TG) analysis was carried using a METTLER TOLEDO TGA/DSC 3+.

#### 2.3. Electrochemical analysis

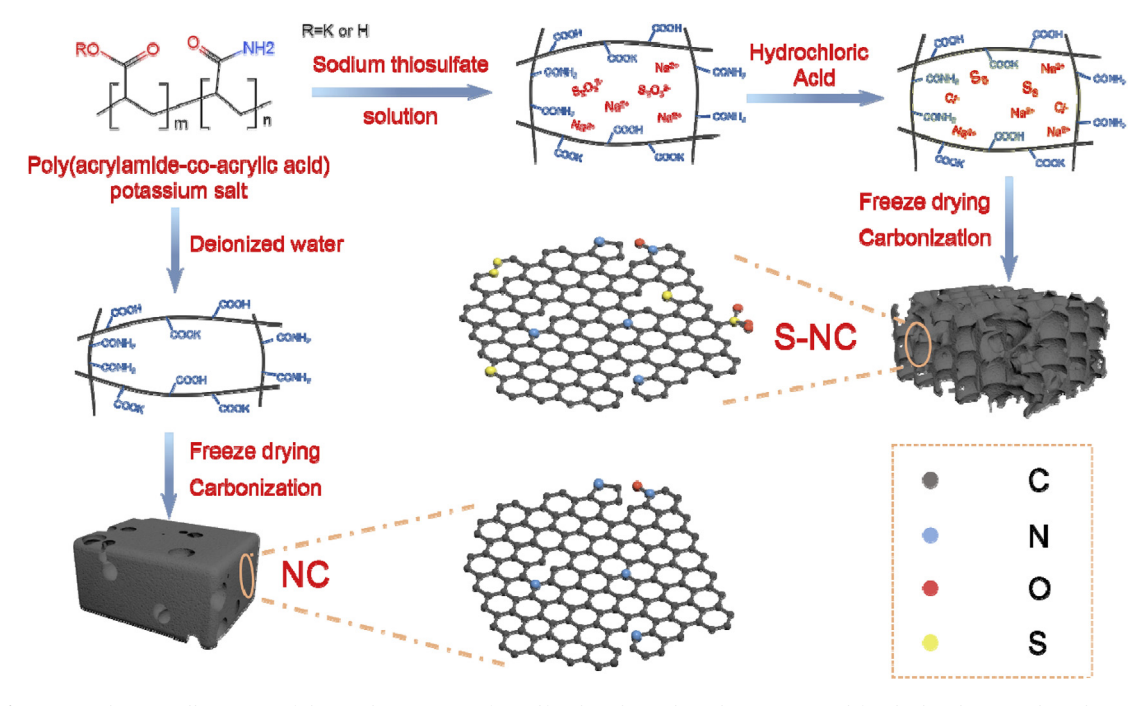
The electrochemical performance of S-NC and baseline NC vs. K/K<sup>+</sup> was examined by employing CR 2032 coin-type cells, which were assembled in an Ar-filled glovebox. To prepare the working electrode, active materials (75 wt%), conductive material (carbon black, 15 wt%), and binder (polyvinylidene fluoride (PVDF), 10 wt%) were dissolved in N-methyl-2-pyrrolidinone to form a slurry, which was pasted onto a copper foil current collector. After being vacuum-dried at 80 °C for 10 h, the electrodes were cut into circular pieces with a diameter of 15 mm, and an average mass loading of  $\sim$ 1.0 mg cm $^{-2}$ . A solution of 0.8 M KPF<sub>6</sub> in ethylene carbonate (EC) and diethyl carbonate (DEC) (1:1 by volume) was employed as the electrolyte. Potassium foil was employed as counter electrodes. Galvanostatic charge-discharge measurements were conducted in the range of 0.001–3.0 V, using a Land CT2001A, battery tester. Cyclic voltammetry (CV), Electrochemical Impedance Spectroscopy (EIS) and Galvanostatic Intermittent Titration Technique (GITT) analysis were performed using a Gamry Interface 1000. All electrochemical measurements were carried out at room temperature.

#### 3. Results and discussion

# 3.1. Synthesis and structure analysis

Scheme 1 illustrates the key steps for synthesis of Sulfur doped N-rich Carbon (S-NC) and baseline N-rich Carbon (NC). While an extended synthesis procedure is provided in the Methods, a brief summary is provided here. Poly (acrylamide-co-acrylic acid) potassium salt is used as carbon precursor to form N-rich carbon framework, while sodium thiosulfate serves as sulfur source. The baseline NC was obtained by directly carbonizing poly (acrylamide-co-acrylic acid) potassium salt. Poly (acrylamide-co-acrylic acid) potassium salt possesses high water absorption capacity because of the hydrophilic groups (-CONH<sub>2</sub>, -COOH and -COOK) [74]. Due to mutual repulsion between carboxylate ions fixed on the polymer chain, the polymer network expands, resulting in internal negative pressure and allowing water to enter the resin [75,76]. The sodium thiosulfate will be uniformly adsorbed by poly (acrylamide-co-acrylic acid) potassium salt. After combining with diluted hydrochloric acid, elemental sulfur is formed while simultaneously giving off sulfur dioxide [77]. The product is heated in sealed N<sub>2</sub> atmosphere at 280 °C for 1 h, followed by carbonization at 800 °C for 2 h. Two more baseline specimens are synthesized, one pyrolyzed at 600 °C and termed S–NC–600, and one pyrolyzed at 1000  $^{\circ}$ C and termed S–NC–1000. These two materials were used to directly investigate the role of N vs. S in electrochemical performance, as detailed subsequently.

Sulfur is liquefied above 115 °C and dispersed inside the pores of the carbon precursor, providing a sulfur-rich environment for the pyrolysis. At 280 °C, carbonization and sulfuration processes will occur simultaneously, being termed *in-situ* sulfuration. This process will be similar to pyrolysis of polyacrylonitrile in the presence of sulfur [78]: Short  $-S_x$ -chains become covalently bonded onto a cyclized carbon backbone, simultaneously dehydrogenating the material to evolve  $H_2S$ . In the subsequent step at 800 °C, the sulfur reacts with the concurrently pyrolyzing carbon to vulcanize the structure. It has been recently shown that upon heating to 1000 °C, covalently bonded S will begin to be eliminated at



Scheme 1. Schematic illustration of the synthesis process for Sulfur doped N-rich Carbon (S-NC) and for the baseline N-rich Carbon (NC).

about 725 °C, much higher temperature than if the S was free or bound inside nanopores [64]. At the 800 °C pyrolysis temperature, some covalently bonded S will be lost. However, as will be demonstrated in the subsequent figures, enough covalently bonded S remains in the structure to favorably affect the electrochemical properties. Were the S present instead as nanoconfined long or short chain molecules, it would have been entirely eliminated at this temperature. Thermogravimetric analysis was employed to confirm the S content of S-NC, with NC as a baseline (Fig. S1). Comparing S-NC and NC allows the weight loss caused by S elimination to be separated from that caused by further pyrolysis. Both S-NC and NC have about 5% weight loss below 130 °C, corresponding to the elimination of adsorbed moisture [64]. At around 200 °C, the weight loss rates for the two materials begin to diverge. The "extra" lower temperature weight loss in S-NC is ascribed to the elimination of unbound elemental sulfur inside the nanopores [79,80]. At 800 °C, the difference in the weight loss for S-NC vs. NC is ~20%, which corresponds to the total eliminated sulfur species.

Fig. 1(a) and Fig. S2 provide SEM micrographs that show the

morphology of S-NC and NC. It may be observed that NC is quite dense as compared to S-NC. In S-NC, the volatilization of excess sulfur at high temperature physically breaks up the carbon, while introducing macroporosity and creating a sheet-like morphology. By contrast, a standard post-pyrolysis particulate-like morphology is formed in the sulfur-free NC. The high-resolution transmission electron microscopy (HRTEM) images confirm the amorphous internal structure of both S-NC and NC, with randomly distributed graphitic ribbons. This is shown in Fig. 1(b) and (c), where there are isolated defective graphene planes in an otherwise amorphous carbon matrix. The lack of long-range order in the carbons is expected due to the low maximum temperature (800 °C) of pyrolysis. Fig. 1(d) shows a high-angle annular dark-field (HAADF) image and the associated C, N, O and S energy-dispersive X-ray Spectroscopy (EDXS) maps of S-NC. Within the resolution of EDXS, the N, O, and S elements are all homogeneously distributed within the carbon.

X-ray diffraction and Raman spectroscopy were employed to investigate the structure of S-NC and the NC baseline. Per Fig. 2(a), S-NC and NC show highly broadened diffraction peaks with  $2\theta$  centered at  $\sim 25^\circ$ .

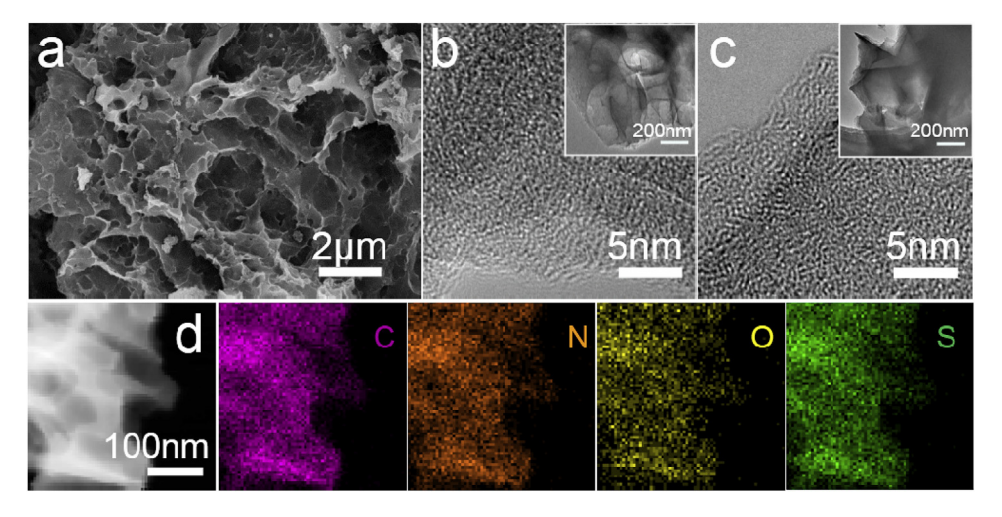


Fig. 1. (a) Representative SEM image for S-NC, with NC being shown on Suppl. (b) and (c) HRTEM images highlighting the disordered structure S-NC and NC, respectively. (d) HAADF image and the corresponding EDXS elemental distributions of C, N, O and S in S-NC.

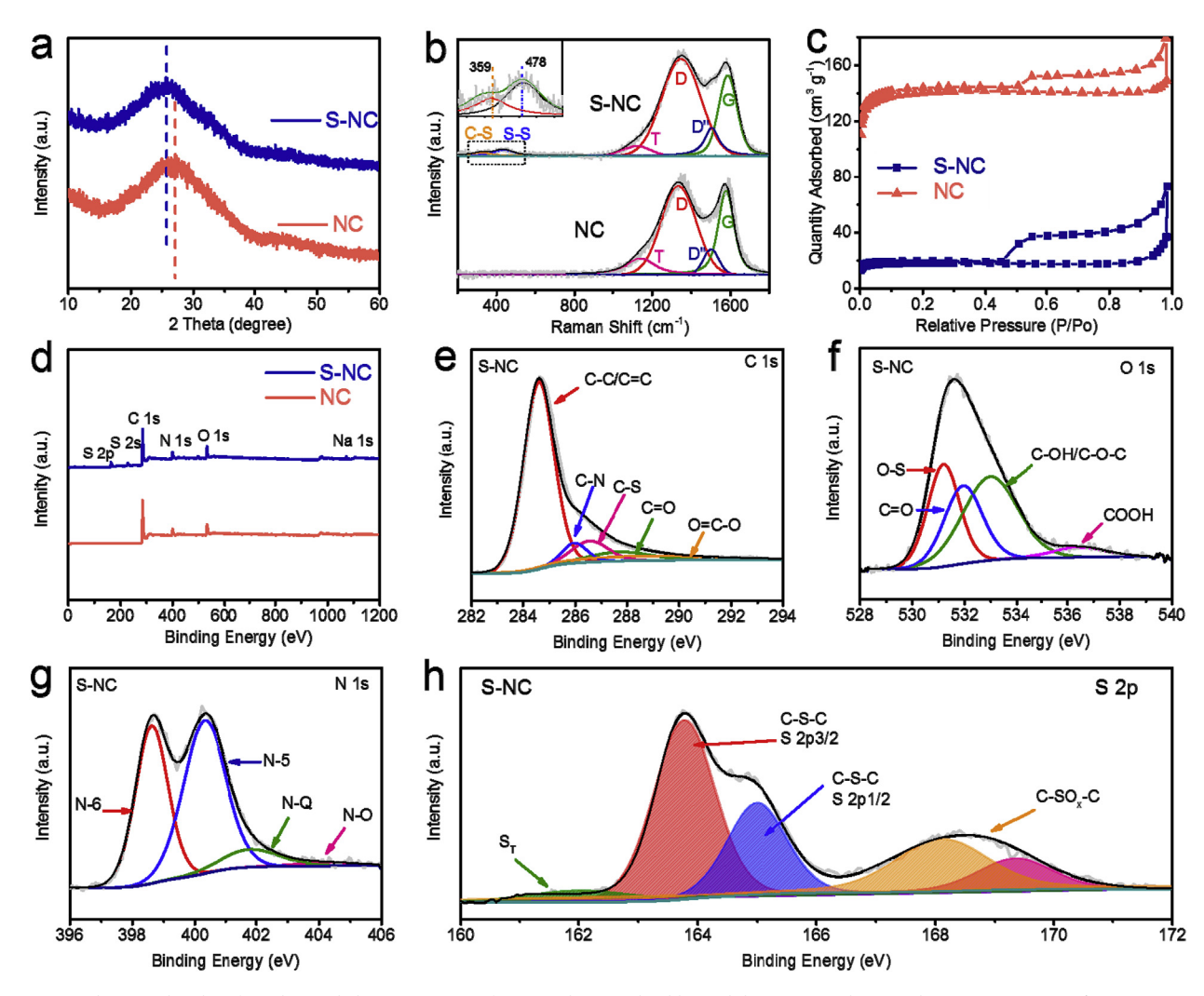


Fig. 2. Structural, textural and surface chemical characterization of S-NC and NC, with additional data presented in Suppl. (a) XRD patterns, (b) Raman spectra, (c) Nitrogen adsorption-desorption isothermal curves, (d) High resolution XPS patterns of S-NC and NC. (e) C1s spectra of S-NC. (f) O 1s spectra of S-NC. (g) N 1s spectra of S-NC. (h) S 2p spectra of S-NC. The associated survey spectra and the high-resolution spectra for NC are shown in Fig. S5-S7.

This (002) type reflection is associated with the average nearest-neighbor spacing between the highly defective graphene layers [81]. Calculated from Bragg's Law, the average graphene layer spacing is found to slightly increase from 0.345nm for NC to 0.352 nm for S-NC, both being wider than the equilibrium 0.3354 nm for graphite.

The Raman spectrum in Fig. 2(b) shows disorder-induced D band at around  $\sim 1350 \text{ cm}^{-1}$  and a graphitic G band at around  $\sim 1580 \text{ cm}^{-1}$ . The D band is related to the breathing mode of k-point phonons, while the G band derives from the conjugated structure of sp<sup>2</sup> carbon [82]. Two additional peaks of at ~1130 cm<sup>-1</sup> (T-band) and at ~1490 cm<sup>-1</sup> (D"-band) are present, being commonly reported for disordered carbons. The former is assigned to disordered graphitic lattice (A1g symmetry) or sp<sup>3</sup>-rich phase, the latter is ascribed to amorphous sp<sup>2</sup>-bonded forms of carbon [83]. The intensity ratio of D band and G band  $(I_D/I_G)$  can be to express the degree of disorder [84,85]. The value of  $I_{\rm D}/I_{\rm G}$  ratio of S-NC and NC are estimated to be 2.33 and 1.83. As expected, sulfur doping results in more structural defects in the carbon, which will lead to more K-active storage sites. Two weak peaks located at 359 and 478 cm<sup>-1</sup> are revealed in S-NC, corresponding to the stretching vibration and deformation of C-S and S-S bonds [86-88]. The observed S-S bond is due to the trapping of small sulfur molecules inside the closed carbon structure.

Nitrogen adsorption-desorption isotherms were employed to analyze the effect of sulfur doping on porosity, per Fig. 2(c). Both S-NC and NC display Type IV isotherms with an obvious hysteresis loop, indicating the

existence of mesopores. The corresponding pore size distribution results were obtained by density functional theory (DFT), as shown in Fig. S3. The pore size distribution results are shown in Table S1. The table indicates that S-NC possesses more macro/mesopores compared to NC. The Brunauer-Emmett-Teller (BET) specific surface area of S-NC is  $56 \text{ m}^2 \text{ g}^{-1}$ , which is much lower than that of NC at 432 m<sup>2</sup> g<sup>-1</sup>. This indicates that there is structural collapse during the high temperature reaction of the pyrolyzing carbon with the S. While small sulfur molecules confined inside gas accessible pores also decrease the specific surface area [86,89], it is highly unlikely than any molecules will survive inside open pores at 800 °C. The reduction of specific surface area in S-NC is a desirable feature, since it should reduce the extent of solid electrolyte interphase (SEI) formation [90,91]. Fig. S4(a) and S4(b) show nitrogen adsorption-desorption isotherms and associated DFT mesopore size distribution of S–NC–600 and S–NC–1000. The specific surface areas are 23 $m^2 g^{-1}$  for S-NC-600 and 113  $m^2 g^{-1}$  for S-NC-1000.

X-ray Photoelectron Spectroscopy was carried out to further investigate the surface chemical composition and chemical bonding in S-NC and NC. Fig. 2(e) shows the high resolution C1s spectra of S-NC. Fig. 2(f) shows the O 1s spectra, Fig. 2(g) shows the N 1s spectra, while Fig. 2(h) shows S 2p spectra. The associated survey spectra and the high-resolution spectra for NC are shown in Fig. S5-S7. The sample S-NC displays prominent peaks corresponding to C 1s, N 1s, O 1s, S 2p and S 2s, as well as a minor peak of Na 1s, per Fig. 2(d). As expected, the S 2s and Na 1s

peaks are absent in NC. Carbon, nitrogen and oxygen are derived from the polymer salt by self-doping, while sulfur is derived from sodium thiosulfate. The residual sodium in S-NC (0.26 at.%) can be ascribed to the addition of sodium thiosulfate.

The spectrum of C 1s contains five peaks located at 284.6, 286.0, 286.5, 287.7 and 291.2 eV, corresponding to the C=C/C-C, C-N, C-S, C=O and O=C-O, respectively [92,93]. The oxygen of S-NC is 8.80 at.%, while it is 9.43 at.% for NC. The O 1s XPS spectra in S-NC corresponds to four functional groups: The covalent bond of O-S (531.2 eV), C=O quinone type groups (O-I, 531.9 eV), C-OH phenol groups and/or C-O-C ether groups (O-II, 533.0 eV), and chemisorbed oxygen (COOH carboxylic groups) and/or water (O-III, 536.5 eV) [94]. The nitrogen content on NC is 8.14 at.%, while it is 9.94 at.% in S-NC, suggesting that S may help to stabilize bound nitrogen during pyrolysis [95]. In the N 1s spectrum, there are peaks at 398.6, 400.3, 401.8 and 404.3 eV. These are attributed to pyridinic nitrogen (N-6), pyrrolic or pyridonic nitrogen (N-5), graphitic nitrogen (N-Q) and oxidized nitrogen (N-O), respectively [96-98]. The N moieties are dominated by N-6 and N-5 species. These can be located at the edges of the defective graphene layers and will thereby introduce extrinsic defects and K active sites to enhance the reversible capacity [66,99]. Due to the S doping, the N-Q/N-6 content

increases from 4.87/38.22% for NC to 7.98/39.63% for S-NC, while N-5 and N-O decreases from 54.74/2.17% to 50.83/1.55%. This indicates that some of the N-5 was converted to N-6 and N-Q by a "ring expansion" model. The increased N-Q specie, located in the carbon layers, can enhance the electronic conductivity of carbons and facilitate charge transfer [100]. Therefore, the fast charge performance of the carbon should be improved. The high-resolution S 2p spectrum of S-NC can be fitted into four main peaks at 163.8, 165.0, 168.1 and 169.3 eV. The two lowest energy peaks are associated with the S 2p3/2/S 2p1/2 (45.01%/22.48%). The peaks at the higher energy are assigned to oxidized-S groups -C-SO<sub>x</sub>-C-, being at 27.97%. This indicates that with of S-NC, sulfur has been successfully incorporated into the carbon structure [101], and being the reason for its survival at 800 °C. The lower energy peak at 161.9 eV, related to terminal sulfur atoms S<sub>T</sub> constitutes only 4.5%. This should correspond to sulfur molecules trapped inside the carbon host (e.g. inside closed pores) and not in open nanoporosity.

The introduced covalently bound sulfur will offer sites for reversible bonding with K ions. Moreover, the incorporation of S into the carbon structure also increases the carbon's electrical conductivity. Four-point probe measured conductivity was 16.8 S m $^{-1}$  for S-NC, versus 6.3 S m $^{-1}$  for NC. This should further enhance the rate capability of S-NC over

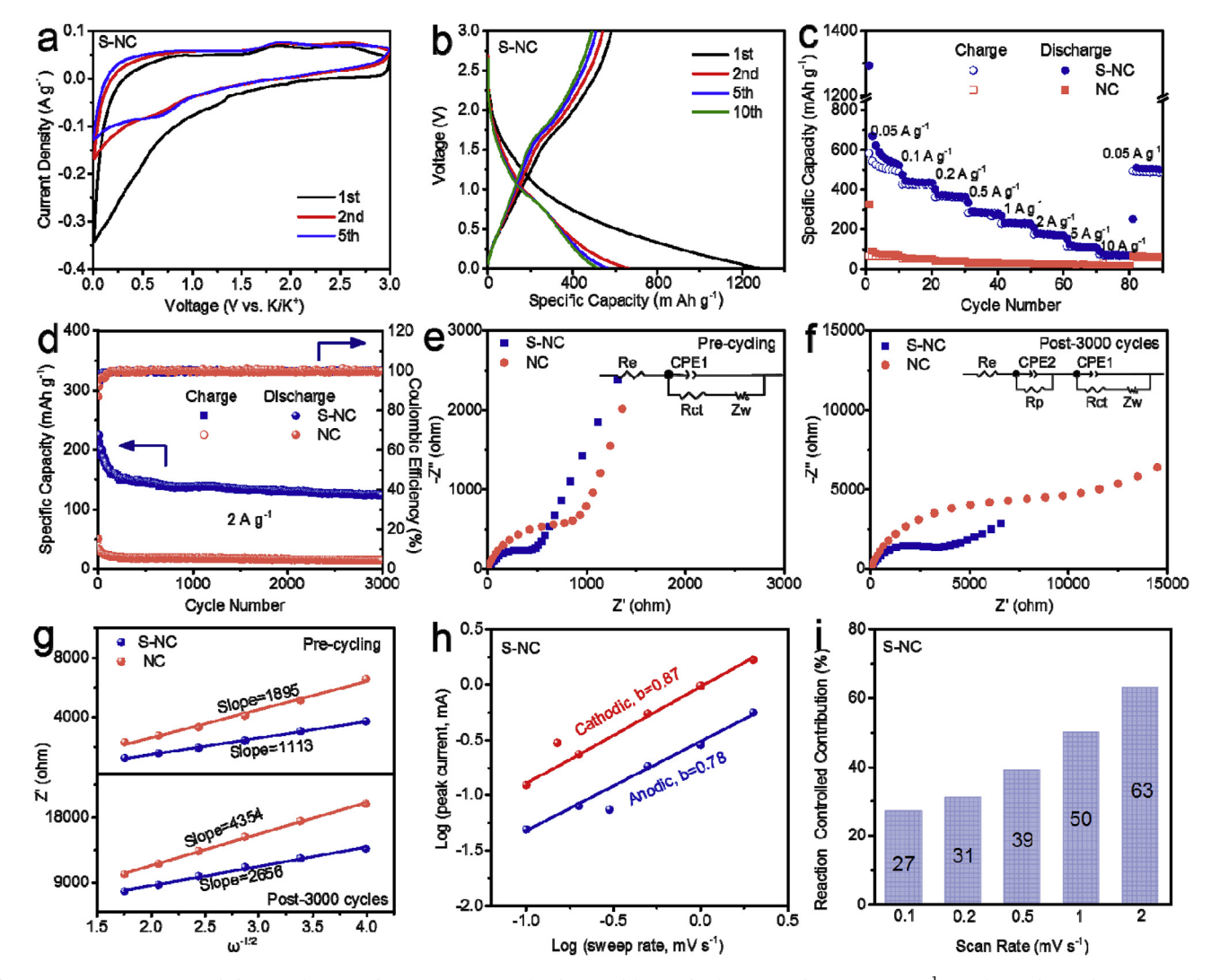


Fig. 3. Potassium-ion storage behavior of S-NC and NC. (a) CV curves for the initial five cycles for S-NC, taken at 0.1 mV s<sup>-1</sup>, CVs for NC being shown in Suppl. (b) Galvanostatic charge-discharge profiles of S-NC at 0.05 A g<sup>-1</sup>, NC being shown in Suppl. (c) Rate capability of S-NC and NC at current densities from 0.05 to 10 A g<sup>-1</sup>. (d) Long-term cycling performance with corresponding CE of S-NC and NC, tested at 2 A g<sup>-1</sup>. EIS Nyquist plots of the S-NC vs. NC, (e) analyzed at cycle 1 and (f) post 3000 cycles, with AC signal of 10 mV (rms) with varying frequencies (0.01–100000Hz), with inset being the equivalent circuit of the EIS fitting. (g) Corresponding linear fits of the Z' versus  $\omega^{-1/2}$  in the low-frequency region. (h) Relation of log of peak current to log of scan rates for S-NC, indicting a linear time dependence (reaction-controlled process) at all rates. (i) Ratio of linear (reaction controlled) vs. square root (diffusion controlled) time dependence at different scan rates.

the NC baseline. The value of  $16.8~S~m^{-1}$  is still relatively low as compared to carbon materials employed for EDLC supercapacitor applications [102,103]. However, for carbon-based potassium ion anodes, solid-state diffusivity within the bulk lattice appears to be the rate-limiting process during intermediate and fast charging [14,27,28]. Authors have reported much more severe bulk diffusion limitations in comparable carbons tested against K versus with Na or Li ions [22,28, 46].

#### 3.2. Potassium storage performance

To evaluate the effects of the doped-S on the electrochemical properties, S-NC as well as the baselines S-NC-600, S-NC-1000 and NC were analyzed as K/K<sup>+</sup> half-cells. Fig. 3(a) provides the CV curves for the initial five cycles for S-NC, taken at 0.1 mV s<sup>-1</sup>. The CVs for NC are shown in Fig. S8(a). In the case of S-NC, the first scan curve shows two irreversible cathodic peaks at about 1.50 and 0.45 V, which can be related to the formation of a solid electrolyte interphase (SEI), as well as some irreversible trapping of K ions in the bulk of the carbon [47,104-105]. In the subsequent cycles, the two reversible redox peaks located at around 0.70/1.80 V are attributed to reversible adsorption of K ions at N/S-containing functional groups [106]. This charge storage mechanism will be examined further in subsequent discussion. By contrast, NC shows a fairly featureless redox profile, comparable to other N and O rich carbons in literature [60,64,107]. The weaker and more broadened cathodic peak at around 0.7 V does indicate the interaction between K ions and N moieties. For the case of S-NC, the close overlap of the 2nd and 5th CV curves reveal the reversibility of the sulfur related charge storage mechanisms. There is more irreversible capacity for NC at cycle one, owing to its larger specific surface area and hence more SEI. In the CV's the cycle 1 Coulombic efficiency (CE) for S-NC is 66.4%, while it is 23.0% for NC. The cycle 1 CE for S-NC is nearly 3X higher than for NC, despite its higher surface area. This result should be directly attributed to the role of S groups in preventing excessive SEI formation. It has been reported that S incorporated into the carbon structure will reduce the degree of SEI formation early in cycling due to the preferential reversible reaction of Li or K ions with S moieties, rather than irreversible reaction with O and OH moieties [63,108,109]. The current findings support this conclusion.

Fig. 3(b) shows the galvanostatic charge-discharge profiles of S-NC at 0.05 A g $^{-1}$ , the corresponding data for NC being shown in Fig. S8(b). For S-NC, there is no obvious voltage platform at  $\sim\!2.2V$ , indicating minimal  $K_2S_n$  ( $5\!\leq\! n \leq 6$ ) polysulfide formation. This would be expected for the S-NC structure which consists of primarily covalently bonded S [64,106]. Due to the 800 °C pyrolysis temperature, the approximate 5% of terminal S in S-NC would have to be sealed off inside the carbon host, for example in closed nanopores. It would therefore not be susceptible to shuttle either, since there would be no direct electrolyte access. Electrolyte soluble polysulfide formation is well-known to be deleterious for extended cycling, due to the ongoing parasitic shuttle that occurs during charging-discharging of the cell. Parasitic shuttle is significant when the S is in its "free" state, i.e. not chemically bound to the carbon, for example being in electrolyte accessible pores [94].

The initial discharge/charge capacities of are 1294 mAh  $\rm g^{-1}/582$  mAh  $\rm g^{-1}$  for S-NC, and 325 mAh  $\rm g^{-1}/64$  mAh  $\rm g^{-1}$  for NC. The galvanostatically measured initial CE for S-NC is 45.0%, while it is 19.7% for NC. Cycling-induced SEI formation is expected to be most severe for materials that undergo large changes in volume during charging-discharging. Also, markedly worse SEI stability has also been reported for bulk insertion of K vs. Na into undoped carbon micro-particulates [64]. While this phenomenon is not fully understood, one can surmise that without heteroatom dopants, most charge storage occurs by ion insertion at geometrically random sites for disordered carbons, or by staging intercalation for graphite and ordered graphenes. In that case there would be volume changes at every cycle, which would destabilize the exiting SEI. The relatively low specific surface area of S-NC significantly improves the initial CE, agreeing with prior reports for a number of

carbons [63,67,110]. A second important cause for the higher initial CE for S-NC is its sulfur content, as discussed. Compared with the previously reported carbon anodes for K ion batteries, the initial CE for S-NC is on-par, being typically above that of carbons with high surface areas [26, 59,65,66,111–113]. This is highlighted in Table S3.

The rate capability of S-NC and NC was investigated through a wide current density range. Fig. 3(c) compares the rate capability of S-NC and NC at current densities from 0.1 to 10 A g $^{-1}$ . The S-NC electrode delivers excellent rate capacity, with reversible capacities of 437, 369, 286, 234, 175, 114 and 72 mAh g $^{-1}$  (at cycle 5) at the current densities of 0.1, 0.2, 0.5, 1, 2, 5 and 10 A g $^{-1}$ . After high rate testing, when the current density is reduced back to 0.05 A g $^{-1}$ , the capacity of S-NC is restored to 502 mAh g $^{-1}$ . This indicates that the redox active S groups are stable at high currents. Overall, the S-NC electrode presents favorable rate capability as compared state-of-the-art carbonaceous anode materials for PIBs [24,45,82,114–116]. These comparisons are shown in Fig. S9 and in Table S3. By contrast, NC presents only 53, 42, 33, 28, 23, 20 and 18 mAh g $^{-1}$  at 0.1, 0.2, 0.5, 1, 2, 5 and 10 A g $^{-1}$ .

Fig. S10(a) directly compares the XPS obtained S and N content of S-NC-600, S-NC and S-NC-1000. The sample S-NC-600 contains 13.1 at.% S and 5.8 at.% N. The sample S-NC contains 12.9 at.% S and 9.9 at.% N. The sample S-NC-1000 contains 5.5 at.% S and 7.2 at.% N. Since the S content in S-NC-600 and S-NC is on-par, the differences in electrochemical performance should be directly attributable to the more significant variation in the N content between the two specimens. Fig. S10(b) and S10(c) show the galvanostatic charge-discharge profiles of S-NC-1000 and S-NC-600 at 0.05 A g<sup>-1</sup>. The initial discharge/charge capacity is  $1181/579 \text{ mAh g}^{-1}$  for S-NC-600 and  $1379/551 \text{ mAh g}^{-1}$  for S-NC-1000, respectively. The initial CE for S-NC-600 is 49.0%, while the initial CE for S-NC-1000 is 40.0%. Fig. S10(d) compares the rate capability of S-NC-600, S-NC, and S-NC-1000 at current densities from 0.05 to  $10~{\rm A}~{\rm g}^{-1}$ . At 0.1, 0.2, 0.5, 1, 2, 5 and  $10~{\rm A}~{\rm g}^{-1}$ , S–NC–600 delivers 311,  $251, 189, 149, 114, 67, 47 \text{ mAh g}^{-1}$ , while S–NC–1000 delivers 260, 207, 153, 115, 79, 41, 21 mAh  $g^{-1}$ . The S-NC anode shows more favorable electrochemical performance than either S-NC-600 or S-NC-1000. Its improvement over S-NC-1000 can be directly ascribed to the higher amount of N (9.9 at.%) in its structure. This result confirms the positive role of N in enhancing K storage capacity and rate capability in defective carbon, supporting the beneficial effect of dual N and S heteroatoms.

Fig. 3(d) shows long-term (3000 cycles) performance and the corresponding CE for S-NC and NC, both tested at 2 A  $\rm g^{-1}$ . S-NC delivers a reversible capacity of 141 mAh  $\rm g^{-1}$  after 3000 cycles, with a capacity decay only 0.01% per cycle, and 75% overall capacity retention. A cycling performance comparison of S-NC versus best PIB carbons from literature is presented in Table S3. It may be concluded that S-NC cycling stability is highly promising. To confirm that there is negligible soluble potassium polysulfide formation during cycling of S-NC, UV-vis spectrum of the post-200 cycles electrolyte was conducted. Fig. S11 shows the UV-vis spectrum of post-cycled electrolyte, with the inset being a photograph of the separator after 200 cycles. It may be observed that the separator is clear and that no potassium polysulfide peaks were observed in the UV-vis spectrum. Both observations confirm that there is negligible soluble potassium polysulfide formation during cycling [117,118].

Most of the capacity fade in S-NC occurred in the first approximately 100 cycles. Key sources of fade are irreversible trapping of K ions at bulk carbon and at heteroatoms, deactivation of K active N sites, and some ongoing SEI formation leading to stresses and limited pulverization of the carbon. Ongoing SEI growth should be a relatively minor contributor at higher cycle numbers, at cycle 11 the CE increases to above 90%, and at cycle 60 it approaches at 100%. The stability of the SEI layer in carbon-based KIB anodes is known to be much more of an issue then for LIB or SIB carbon anodes [28,48,119-120]. Fig. S12 shows SEM analysis of the S-NC electrode after 1st and 5th cycle charge-discharge cycle at 0.05 A g<sup>-1</sup>. The analysis includes imaging and EDXS mapping of C, N, O, K, F, P and S. After first cycle, the surface of the S-NC is covered by a uniform SEI layer. After cycle 5 the morphology of the specimen fairly analogous,

indicating that while additional SEI has formed, the growth has not been severe. The EDXS maps reveal K, C, S, O, N, P and F elements at both cycle 1 and cycle 5. Since S is not a known constituent of the SEI, its signal must originate from the underlying carbon. The lower relative intensity of S after cycle 5 than at cycle 1, indicates SEI growth. However, the S signal is still relatively strong, indicating that the SEI growth in S-NC is limited after cycle 1. The calculated weight percentages of these elements are presented in Table S4. The P and F signals could be just some PF6 which are not washed off. The increased K and O derived from the SEI growth, such as potassium oxide, potassium carbonates, potassium alkyl carbonates, etc. which can be related to the decomposition of ester solvent and salt [119]. Fig. S13 shows TEM and HRTEM images of the disassembled S-NC electrode after 1st and the 5th cycles. The amorphous S-NC and the SEI give sufficiently similar mass-thickness contrast (plus beam damage effects) that it is not possible to quantitatively analyze the SEI. However, qualitatively it may be observed that the surface of the S-NC specimens is fairly analogous, agreeing with the SEM results.

To investigate a full device application of S-NC, potassium hybrid ion capacitor (PHIC) was fabricated by using S-NC as the anode and an ion adsorption nanocage carbon cathode, termed "NFCNs-800". Detailed synthesis and characterization of NFCNs-800 can be found in the previous work [121]. The electrochemical performance of the NFCNs-800 cathode can be found in Fig. S14(a) and (b). Before assembling the device, the S-NC anode and NFCNs-800 cathode were firstly activated at 0.1 A g $^{-1}$  for 3 cycles. The anode to cathode mass ratio employed was 1:1, with an average mass loading of  $\sim\!1.0$  mg cm $^{-2}$  (same as for half-cells). The working voltage window of the NFCNs-800//S-NC was selected in the range of 0–4 V. Fig. 4(a) and 4(b) show the CV curves and the galvanostatic discharge-charge profiles of the hybrid device, while Fig. 4(c) presents the Ragone plot. The specific energy (*E*, Wh kg $^{-1}$ ) and specific power (*P*, W kg $^{-1}$ ) were based on the total mass of both anode and cathode materials, being calculated using the following equations:

$$\Delta V = (V_{\text{max}} + V_{\text{min}})/2 \tag{1}$$

$$P = \Delta V \times i \tag{2}$$

$$E = P \times t/3600 \tag{3}$$

where t (s) is the discharge time in sec., i (A g<sup>-1</sup>) is the charge/discharge current,  $V_{max}$  and  $V_{min}$  are voltages at the beginning and the end of discharge excluding the IR drop (V). The as-built PHIC delivers the optimal energy density of 110 Wh kg<sup>-1</sup> at 244 W kg<sup>-1</sup>, which is comparable to the state-of-the-art K-based hybrid energy storage devices [36, 122–125]. Per Fig. 4(d), the NFCNs-800//S-NC device presents an impressive cycling stability for K-based system, with a capacity retention of 86.4% over 3000 cycles at a current density of 5 A g<sup>-1</sup>.

Electrochemical impedance spectroscopy analysis was employed to further understand the changes in S-NC and baseline NC, the samples being analyzed at cycle 1 and after 3000 cycles with an alternating current (AC) signal of 10 mV (rms) with varying frequencies (0.01–100000Hz). These results are shown in Fig. 3(e)-3(g). The values of equivalent series resistance  $R_{\rm e}$  (primarily related to electrolyte resistance) and charge transfer resistance  $R_{\rm ct}$  (which contains both charge transfer and SEI contribution) can be obtained by fitting the Nyquist plots with the equivalent circuit shown in the inset of Fig. 3(e) and (f) [126]. For S-NC, the values of  $R_{\rm ct}$  increase from 510  $\Omega$  to 4397  $\Omega$  after 3000 cycles. For NC these values go from 1150  $\Omega$  to 11520  $\Omega$ , being consistent with its higher surface area and greater SEI formation tendency.

The Warburg impedance  $Z_{\rm w}$  corresponds to the sloping line in the low frequency region and related to the K<sup>+</sup> diffusion process. In Warburg region, the values of  $D_{\rm K}$  (diffusion coefficient of K<sup>+</sup>) can be calculated via Equation (4) [127,128].

$$D_{K} = \frac{R^{2}T^{2}}{2A^{2}n^{4}F^{4}C^{2}\sigma^{2}} (\sigma = \frac{dZ'}{d\omega^{-1/2}})$$
(4)

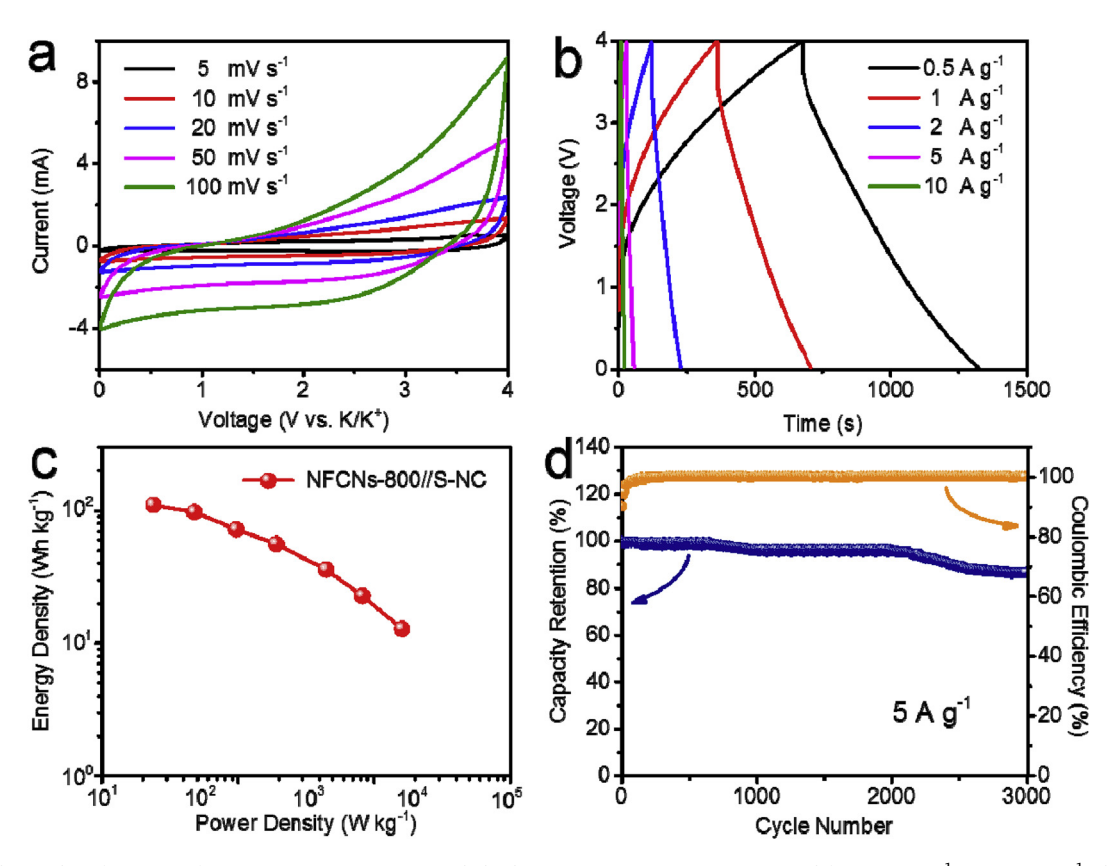


Fig. 4. Electrochemical performance of NFCNs-800//S-NC potassium hybrid ion capacitor. (a) CV curves tested from 5 mV s<sup>-1</sup> to 100 mV s<sup>-1</sup>. (b) Representative galvanostatic discharge-charge profiles at different current densities. (c) Ragone plot of NFCNs-800//S-NC. (d) Cycling stability of NFCNs-800//S-NC at 5 A g<sup>-1</sup>.

where *R*, *T*, *A*, *n*, *F*, *C* and  $\sigma$  are respectively, the gas constant, the absolute temperature, the active surface area of the electrode/electrolyte interface, the number of the transferred electrons, the Faraday constant, the bulk concentration and the Warburg coefficient. The  $D_K$  value of S-NC electrode is  $3.3 \times 10^{-17}$  cm $^2$  s $^{-1}$ , which is higher than that of NC at  $1.2 \times 10^{-17}$  cm $^2$  s $^{-1}$ . After 3000 cycles, the  $D_K$  value of S-NC decreases to  $5.7 \times 10^{-18}$  cm $^2$  s $^{-1}$ , while for NC it decreases to  $2.3 \times 10^{-18}$  cm $^2$  s $^{-1}$ . These changes may be related to a more tortuous solid-state diffusion path for the K ions due to irreversible trapping and deactivation of some sites.

The potassiation kinetics in S-NC were further analyzed. Specifically, the goal was to separate reaction-controlled and hence facile charge storage from bulk-diffusion controlled charge storage that is intrinsically more sluggish. A series of electroanalytical testes were carried out for both materials. A series of CV tests were conducted at various scan rates  $(0.1-2.0 \text{ mV s}^{-1})$ , these being shown in Fig. S15(a) and S15(b). The cathodic and anodic peaks display substantial distortion with the increasing scan rates, indicative of polarization effects [64]. To account for this, the maximum (peak) current was employed to calculate the anodic and cathodic *b*-values. The relationship between measured current (*i*) and scan rate ( $\nu$ ) can be calculated by the following equation:

$$i = av^b (5)$$

where a and b are adjustable parameters [129,130]. The values of b-exponent are determined by the slope of the  $\log(i)$  vs.  $\log(\nu)$ . The result of this analysis is presented in Fig. 3(h) and Fig. S15(c).

Accordingly, the *b*-value close to 1 indicates a linear time dependence of maximum reaction rate. Such charge storage process is reaction-controlled, *i.e.* Activation Polarization limited. While often this is attributed to a "surface capacitive process", it does not necessarily mean EDLC charge storage. Certainly, for either S-NC or NC there is not enough electroactive surface area to have significant EDLC contribution to capacity. Rather, a linear time dependence can indicate a number of surface or bulk reaction-limited processes. These would be based on both faradaic charge transfer between the K ions and the S/N moieties, and on reversible adsorption of K ions at defects. Any charge-storage process which is not diffusion limited would have a time<sup>1</sup> rather than time<sup>1/2</sup> dependence. Even classical bulk solid-state phase transformations may be reaction, rather than diffusion controlled [131].

For time<sup>1/2</sup> dependence, the *b*-value is close to 0.5 and well correlates to a diffusion-controlled process [116]. With graphite, this is the classic solid-state diffusion-limited ion intercalation staging reaction [23,132]. However, there is not enough graphitic order in either S-NC or NC as to allow for orderly K staging. Therefore, a time<sup>1/2</sup> dependence will signal some other form of Concentration Polarization process, such as K ion insertion into energetically favorable but geometrically random bulk sites. Especially for K ion insertion into both graphic and non-graphitic carbons, solid-state limited process are reported to be kinetically sluggish [64,133]. The calculated cathodic *b*-values are 0.87 for S-NC and 0.81 for NC, indicating the kinetics being closer to reaction-controlled. These results are shown in Fig. 3(h) and Fig. S15(c). The calculated anodic *b*-values are 0.78 for S-NC and 0.88 for NC, also confirming a primarily reaction-controlled process. These results are shown in Fig. 3(h) and Fig. S15(c).

The reaction controlled versus solid-state diffusion controlled contributions to the total reversible capacity in S-NC and NC were further quantitatively analyzed using the following equation:

$$i(v) = i_{React} + i_{Diff} = k_1 v + k_2 v^{1/2}$$
 (6)

with  $k_1$  and  $k_2$  as adjustable parameters related to reaction and bulk diffusion processes, respectively [134,135]. By plotting  $i/v^{1/2}vs.v^{1/2}$ , the values of  $k_1$  and  $k_2$  can be determined from the slope and intercept. For S-NC, the ratio of reaction controlled capacity contribution to diffusion-controlled capacity contribution increase from 27% at 0.1 mV s<sup>-1</sup>, to 31% at 0.2 mV s<sup>-1</sup>, 39% at 0.5 mV s<sup>-1</sup>, 50% at 1 mV s<sup>-1</sup> and 63% at 2 mV s<sup>-1</sup>. These findings are shown in Fig. 3(i). For NC, the ratio of

reaction controlled capacity contribution to diffusion-controlled capacity contribution increase from 45% at 0.1 mV s $^{-1}$ , to 52% at 0.2 mV s $^{-1}$ , 61% at 0.5 mV s $^{-1}$ , 69% at 1 mV s $^{-1}$  and 77% at 2 mV s $^{-1}$ . These findings are shown in Fig. S15(d). A higher relative fraction of kinetic controlled processes for NC is consistent with its high surface area which is expected to contribute to the total capacity through ion reversible absorption (not EDLC) at surface heteroatom groups and defect sites.

Galvanostatic Intermittent Titration Technique was employed to analyze the K ion diffusivity ( $D_K$ ) in the S-NC and NC specimens through the entire range of relevant voltages. The GITT data of S-NC and NC were recorded at a constant current density of 25 mA g<sup>-1</sup> for an interval of 30 min followed by 180 min relaxation in the first cycle. Fig. 5(a) presents the GITT curves of S-NC and NC, with the inset schematic illustrating the calculation for  $D_K$ . Fig. 5(b) and (c) presents the  $D_K$  value of S-NC and NC electrodes, calculated using the standard approach based on Fick's second law and Equation (7) [136,137].

$$D_K = \frac{4}{\pi \tau} \left(\frac{m_B V_M}{M_b S}\right)^2 \left(\frac{\triangle E_s}{\triangle E_\tau}\right)^2 \tag{7}$$

where  $\tau$  is the pulse time;  $m_B$  is the mass of the active material; S is the geometric area of the electrode;  $V_M$  is the molar volume of the electrode materials;  $M_B$  is the molar mass of carbon, and  $\Delta E_s$  and  $\Delta E_t$  are defined as shown in Fig. 5(a).

For S-NC, at potassiation voltages of 2.6, 1.2, 0.5, 0.2 and 0.15 V, the values of  $D_{\rm K}$  are  $2.7 \times 10^{-11}$ ,  $2.2 \times 10^{-12}$ ,  $1.8 \times 10^{-12}$ ,  $1.9 \times 10^{-13}$ , 6.0  $\times$  10<sup>-14</sup> cm<sup>2</sup> s<sup>-1</sup>. For NC potassiated to the same voltages, the  $D_K$  values are 3.6  $\times$  10<sup>-12</sup>, 7.3  $\times$  10<sup>-13</sup>, 4.3  $\times$  10<sup>-13</sup>, 1.7  $\times$  10<sup>-13</sup> and 2.3  $\times$  10<sup>-13</sup> cm<sup>2</sup> s<sup>-1</sup>, respectively. The  $D_K$  for S-NC shows a continuous decline, especially at below 0.5 V. The  $D_K$  of NC also presents a similar trend, although not to the same severe extent. The decreasing diffusivity with higher K content may be rationalized in terms of a distribution of ion binding energies: The ion storage sites at the lowest voltage correspond to the least negative binding energy ( $\Delta G = - nFE$ ), with the least driving force for their occupancy. During potassiation, there are progressively more saturated K-S, K-N groups and K-carbon defect products in the lattice, leaving less sites available for additional K ions to diffuse into. During depotassation the trend is opposite: The ion diffusivity starts at a maximum and decreases as the samples are depotassiated to higher voltages. This supports the proposed relationship between diffusivity and binding site energy. The weakest bound ions are the most facile to extract and hence possess the highest diffusivity out of the material. During the depotassiation process of S-NC, at 0.2, 0.5, 1, 1.6 and 2.2 V, the  $D_{\rm K}$  values are 2.0  $\times$  10<sup>-11</sup>, 4.9  $\times$  10<sup>-12</sup>, 6.1  $\times$  10<sup>-12</sup>, 9.2  $\times$  10<sup>-13</sup>, 6.1  $\times$  10<sup>-13</sup> cm<sup>2</sup> s<sup>-1</sup>. For NC these values are 2.4  $\times$  10<sup>-12</sup>, 1.0  $\times$  10<sup>-12</sup>, 1.2  $\times$  10<sup>-12</sup>, 2.0  $\times$  $10^{-13}$  and  $2.3 \times 10^{-13}$  cm<sup>2</sup> s<sup>-1</sup>, respectively. This indicates that depotassiation  $D_{\rm K}$  of S-NC is a factor of 2.7–8.3 higher than for NC. Qualitatively, these results and the associated explanation agree with findings of Wu et al., who observed similar trends in potassium diffusivities for intercalation vs. deintercalation into ordered graphite [120]. One difference with the current study, however, is that S-NC is far too disordered to form staging compounds such as KC<sub>24</sub>, KC<sub>16</sub>, etc. reported by the authors.

To obtain in-depth insight into the potassiation/depotassiation mechanisms in S-NC, *post-mortem* XPS analysis was carried out. The specimens were disassembled at different states of charge during the first and the second cycle. These results are shown in Fig. 6 and in Fig. 7. All the disassembling, storage and transfer steps were performed in inert Ar atmosphere, ensuring minimal oxidation-related artifacts. Fig. 6 presents a summary of the XPS analysis of S-NC analyzed at different potassium insertion/extraction voltages, at cycle 1 and cycle 2. Fig. 6(a) shows the voltages at which XPS analysis was performed, bottom panel being for cycle 1, top panel being for cycle 2. At cycle one, specimens are analyzed in their pristine state (I), at 1 V (II), 0.2 V (III), 0.001 V (IV), 1.5 V (V), and 3 V (VI). At cycle two, specimens were analyzed at 3 V (VI) *i.e.* same analysis as cycle one, at 0.001 V (VII), and 3 V (VIII). The current density

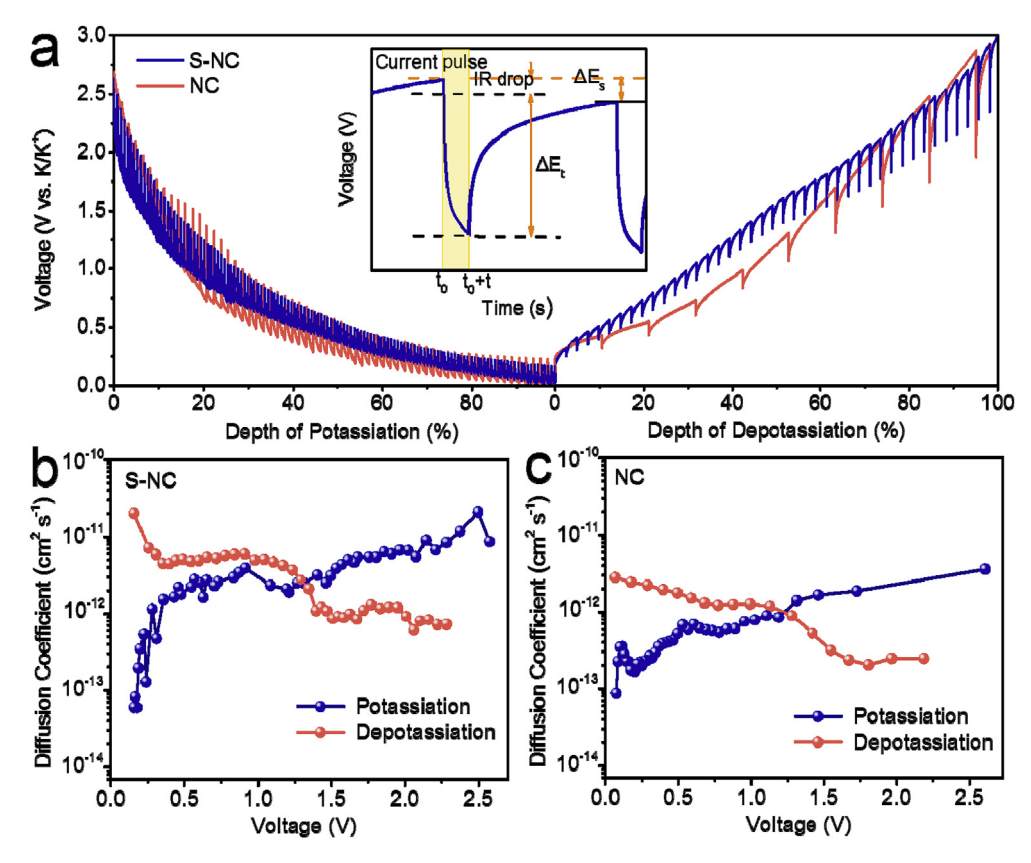


**Fig. 5.** (a) GITT curves of S-NC and NC at 0.001–3 V, with inset being a schematic for the calculation method employed. The analysis was based on an applied current of 25 mA g<sup>-1</sup> for 0.5 h, followed by a 3 h relaxation. (b) and (c) The solid-state diffusion coefficients of K ions for S-NC vs. NC, calculated at different voltages during potassiation and during depotassiation.

employed for this analysis was  $0.05~{\rm A~g^{-1}}$ .

Fig. 6(b) shows the high resolution K 2p XPS spectra. Fig. 6(c) shows the S 2p XPS spectra, while Fig. 6(d) shows the N 1s XPS spectra. The survey spectrum is shown in Fig. 7 and Fig. S16. At a potassiation voltage of 1 V, peaks at 293.2 eV and at 296 eV are present in K 2p spectra. This indicates the presence of K–C bonds [63]. Since S-NC is too disordered to allow for K intercalation, the K–C bonds can be attributed to adsorption

of K ions at various carbon chemical and structural defects. When the potassiation voltage reaches 0.2 V, the above two peaks shift to a lower binding energy ( $E_b$ ), while increasing in overall intensity. At 0.001V, these peaks shift to the lowest binding energy while achieving their maximum intensity. During the subsequent depotassiation process, the two peaks recover to higher  $E_b$  values while reducing in their intensity. However, even at 3 V some K–C peak intensity is still present. This is due

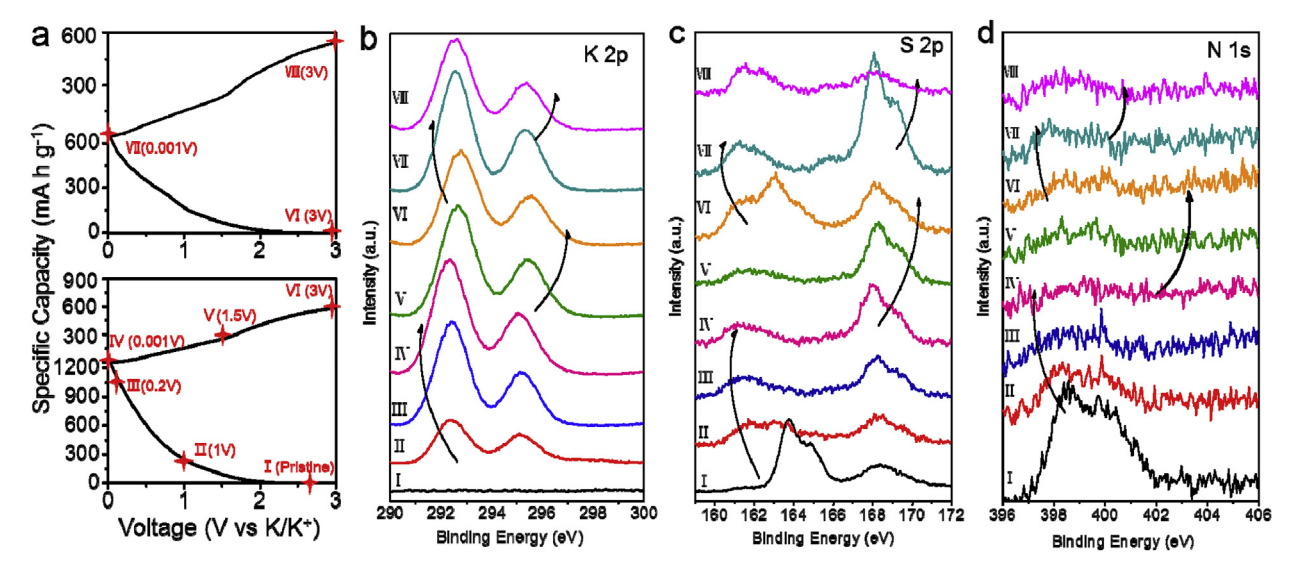


Fig. 6. Post-mortem XPS analysis of S-NC at different potassiation/depotassiation voltages, during cycle 1 and cycle 2. (a) Corresponding voltages where analysis was performed, bottom panel is cycle 1, top panel is cycle 2. (b) High resolution K 2p XPS spectra. (c) S 2p XPS spectra. (d) N 1s XPS spectra. The survey spectrum is shown in Suppl.

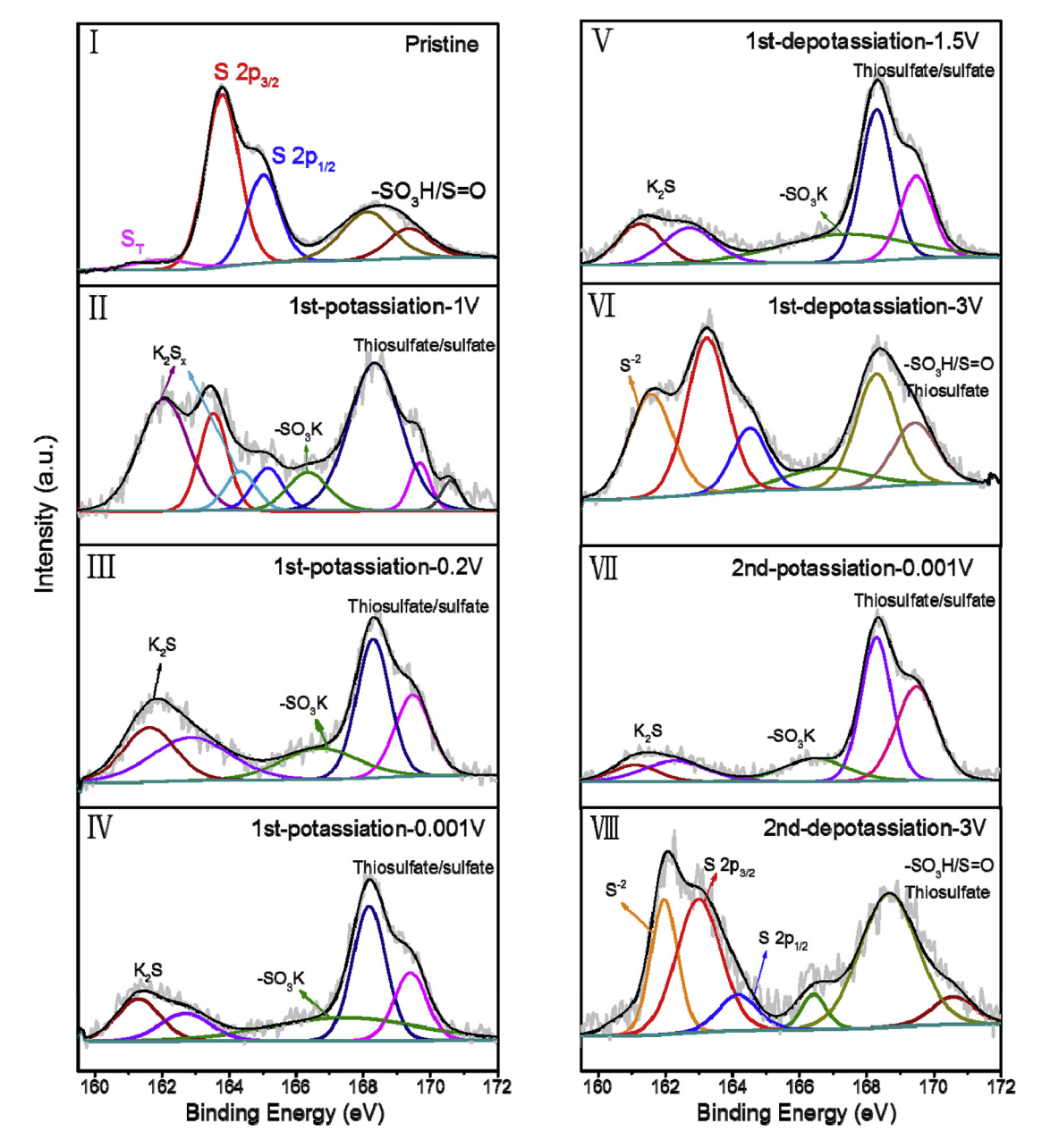


Fig. 7. Deconvoluted S 2p peaks of the S-NC electrode at different potassiation/depotassiation voltages, during cycle 1 and cycle 2.

to limited irreversible trapping of K in the carbon matrix, as discussed earlier. During cycle two potassiation the binding energy of the K 2p peaks likewise decreases, while their intensity increases. The reverse trend is observed during cycle two depotassiation. These largely reversible changes in  $E_b$  indicate that the potassiation reactions with the carbon matrix are reversible.

The evolution of S chemical bonds with K was also analyzed by XPS. These results are shown in Figs. 6(c) and Fig. 7. The S 2p peak at initial state can be divided into four different peaks located at 163.8, 165.0, 168.1 and 169.3 eV, which were assigned to S 2p3/2, S 2p1/2 and -S-Ox-S, respectively. At a potassiation voltage of 1 V, it can be seen that the S 2p3/2 and S 2p1/2 peaks still exist. Moreover, two additional peaks appear at 161.3/162.6 eV, being related to the formation of sulfides ( $K_2S_x$ ). The three peaks located in the higher  $E_b$  can be related to thiosulfate and sulfate [78,138]. When the potassiation voltage reaches to 0.2 V, the intensity of S 2p3/2 and S 2p1/2 peaks decreases and those two peaks disappear. At the terminal voltage of 0.001 V, the two distinct peaks at 161.3/162.8 eV assigned to sulfides ( $K_2S$ ), indicating the step

reactions of S and K. In the fully potassiated state, the E<sub>b</sub> of S 2p negatively shifted to a lower value at fully potassiation state, indicating that the strong interaction of K<sup>+</sup> and S atoms lead to a lower valence state of S [139]. At cycle one depotassiation voltage of 1.5 V, there are no obvious changes in the S-related spectra versus when in the terminally potassiated state. This indicates that minimal K-S reaction occurs in this voltage range during the first anodic charge. During depotassiation to higher voltages, the intensity of S 2p gradually increases, while the intensity of the sulfur-oxygen functional group gradually decreases. At 3V, the binding energy of S 2p3/2 and S 2p1/2 shifts to 163.2 and 164.8 eV, indicating reversible oxidation of S [69]. However these energy values remain lower than those of the pristine sample, which were at 163.8 and 165.0 eV, indicating that some S reduction is not reversible. The peak at 162.1 eV is assigned to the residual sulfide species ( $S^{2-}$ ), which would arise from the incomplete oxidation reaction [140]. The peaks for -SO<sub>3</sub>Hand other sulfur oxygen functional groups are also stronger than in the pristine sample. This is also ascribed to irreversible electrochemical reactions at cycle 1. At cycle two potassiation to 0.001 V, the two distinct  $K_2S$  peaks at 161.3/162.8 eV reappear, as well as do the thiosulfate and sulfate peaks. In addition, the  $S^{2-}$  and S 2p peaks replace  $K_2S$  peaks and  $-SO_3H/S = O$  peaks appear after cycle two depotassiation.

Fig. 6(d) presents the XPS N 1s spectra. The XPS results reveal what occurs during the potassiation-depotassiation process for the various N moieties. While the sodiation reactions with N functional groups have been considered prior [141], to our knowledge there has not been a systematic analysis of potassiation reactions. At cycle one potassiation to 1 V, the N-6, N-5 and N-Q start to react with K<sup>+</sup>, while N-O does not react with K<sup>+</sup> (per. Fig. S16). When the potassiation reaches 0.2 V, the N-5 and N-6 groups react with K<sup>+</sup> and are no longer discernable. The moiety N-Q is not fully reacted, while N-O just begins to react. At the terminal 0.001 V, all the N configurations appear to have reacted. The  $E_b$  of N-6, N-5, N-Q, and N-O negatively shifts from the original values of 398.8, 400.3, 401.3, and 403.5 eV to 398.3, 399.2, 400.3, and 403.4 eV, respectively. This indicates that charge was transferred from K to the N-dopants, to form K-protonated N structures in the carbon matrix. During the subsequent depotassiation process, some of the nitrogen-containing functional group do not return to the original state. Specifically, N-6 and N-5 don't reappear, rather forming a product that could not be readily identified. However, the N-O and N-O groups do reform upon depotassiation. This may be observed in the cycle one depotassiation 1.5 V and 3 V spectra.

At cycle two potassiation to 0.001 V, the N-5/K and N-6/K peaks nearly have no change, while N-Q and N-O all transform into N-Q/K and N-O/K, respectively. At depotassiation to 3V, the N-Q and N-O peaks reappear, while N-5/K, N-6/K and N-Q/K still exist. According to the above analysis, the reaction of N with  $\rm K^+$  is a gradual process. The reaction of N-6/5 to another configuration appears irreversible. However at least a portion of the reaction of N-Q and N-O is fully reversible in the sense that these functional groups are recovered. In summary, the N and N-O related peaks undergo a series of complex shifts that indicate both reversible and irreversible changes to the functional group structure. It is important to note that the irreversible changes described above do not necessarily mean that the capacity is lost, only that the functional groups do not revert to their original configuration. Although the electrochemical potassiation reaction is largely reversible, the type N-C bonds that exist afterward are not the fully same as in the starting material.

#### 4. Conclusions

For KIB carbon-based anodes, it is extremely challenging to achieve a combination of high capacity, rate capability and cycling life, especially in dense materials. Here we synthesize and test a low-surface area (56 m<sup>2</sup> g<sup>-1</sup>) S and N-rich carbon that simultaneously achieves all three criteria. The carbon termed S-NC, delivers 437, 369, 286, 234, 175, 114 and 72 mAh  $\mathrm{g}^{-1}$  at 0.1, 0.2, 0.5, 1, 2, 5 and 10 A  $\mathrm{g}^{-1}$ . Upon extended testing (3000 cycles) it decays by only 0.01% per cycle. Such performance is due to the material's unique structure based on covalently bonded, rather than "free", sulfur combined with a range of nitrogen moieties. A broad comparison with the state-of-the-art KIB anode carbons literature indicates that this combination of capacity-fast charge capability-cycling life is highly favorable. The role and the voltage-dependent evolution of S and N functional groups is examined in detail, employing postmortem XPS as well as GITT and EIS analyses. The resultant detailed findings highlight the complex interplay of S and N heteroatoms in boosting the electrochemical performance of carbons used as negative electrodes.

# **Declaration of competing interest**

The authors declare that they have no known competing financial interests or personal relationships that could have appeared to influence the work reported in this paper.

#### CRediT authorship contribution statement

Lin Tao: Methodology, Data curation, Investigation, Writing - original draft. Yunpeng Yang: Conceptualization, Methodology, Investigation. Huanlei Wang: Supervision, Funding acquisition, Resources, Writing - review & editing. Yulong Zheng: Software, Visualization. Hongchang Hao: Writing - review & editing. Wenping Song: Visualization. Jing Shi: Conceptualization, Supervision. Minghua Huang: Funding acquisition, Writing - review & editing. David Mitlin: Conceptualization, Funding acquisition, Supervision, Writing - review & editing.

#### Acknowledgements

L.T., Y.Y., H.W., Y.Z., W.S., J.S., M.H. (conception of research, synthesis and experimental analysis, co-preparation of manuscript) were supported by the Shandong Provincial Key R&D Plan and the Public Welfare Special Program, China (2019GGX102038), the Fundamental Research Funds for the Central Universities (No. 201822008 and 201941010), the Qingdao City Programs for Science and Technology Plan Projects (19-6-2-77-cg), the National Natural Science Foundation of China (No. 21775142 and 21471139), and the Sino-German Center for Research Promotion (Grants GZ 1351). H.H., D.M. (co-conception and guidance of research, preparation of manuscript) was supported by the National Science Foundation, Civil, Mechanical and Manufacturing Innovation (CMMI), Award Number 1911905.

#### Appendix A. Supplementary data

Supplementary data to this article can be found online at https://do i.org/10.1016/j.ensm.2020.02.004.

#### References

- G.L. Soloveichik, Battery technologies for large-scale stationary energy storage, Annu. Rev. Chem. Biomol. Eng. 2 (2011) 503–507.
- [2] Y. Liu, Z. Tai, Q. Zhang, H. Wang, W.K. Pang, H.K. Liu, K. Konstantinov, Z. Guo, A new energy storage system: rechargeable potassium-selenium battery, Nano Energy 35 (2017) 36–41.
- [3] A. Manthiram, A. Vadivel Murugan, A. Sarkar, T. Muraliganth, Nanostructured electrode materials for electrochemical energy storage and conversion, Energy Environ. Sci. 1 (2008) 621–638.
- [4] H. Yang, R. Xu, Y. Yu, A facile strategy toward sodium-ion batteries with ultralong cycle life and high initial Coulombic Efficiency: free-standing porous carbon nanofiber film derived from bacterial cellulose, Energy Storage Mater 22 (2019) 105–112
- [5] R. Krishnan, T.M. Lu, N. Koratkar, Functionally strain-graded nanoscope for high power Li-ion battery anodes, Nano Lett. 11 (2011) 377–384.
- [6] S. Mukherjee, A. Banwait, S. Grixti, N. Koratkar, C.V. Singh, Adsorption and diffusion of lithium and sodium on defective rhenium disulfide: a first principles study, ACS Appl. Mater. Interfaces 10 (2018) 5373–5384.
- [7] P.J. Kim, K. Kim, V.G. Pol, A comparative study of cellulose derived structured carbons on the electrochemical behavior of lithium metal-based batteries, Energy Storage Mater 19 (2019) 179–185.
- [8] A.K. Budumuru, B. Rakesh, C. Sudakar, Enhanced high rate capability of Li intercalation in planar and edge defect-rich MoS<sub>2</sub> nanosheets, Nanoscale 11 (2019) 8882–8897.
- [9] Y. Liang, W.H. Lai, Z. Miao, S.L. Chou, Nanocomposite materials for the sodiumion battery: a Review, Small 14 (2018), 1702514.
- [10] X. Niu, Y. Zhang, L. Tan, Z. Yang, J. Yang, T. Liu, L. Zeng, Y. Zhu, L. Guo, Amorphous FeVO<sub>4</sub> as a promising anode material for potassium-ion batteries, Energy Storage Mater 22 (2019) 160–167.
- [11] M. Keller, C. Vaalma, D. Buchholz, S. Passerini, Development and characterization of high-performance sodium-ion cells based on layered oxide and hard carbon, Chem ElectroChem 3 (2016) 1–10.
- [12] L. Qin, Y. Lei, H. Wang, J. Dong, Y. Wu, D. Zhai, F. Kang, Y. Tao, Q. Yang, Capillary encapsulation of metallic potassium in aligned carbon nanotubes for use as stable potassium metal anodes, Adv. Energy Mater. 9 (2019), 1901427.
- [13] Y. Li, L. Zhang, S. Liu, X. Wang, D. Xie, X. Xia, C. Gu, J. Tu, Original growth mechanism for ultra-stable dendrite-free potassium metal electrode, Nano Energy 62 (2019) 367–375.
- [14] A. Eftekhari, Z. Jian, X. Ji, Potassium secondary batteries, ACS Appl. Mater. Interfaces 9 (2017) 4404–4419.
- [15] Z. Zhao, Z. Hu, R. Jiao, Z. Tang, P. Dong, Y. Li, S. Li, H. Li, Tailoring multi-layer architectured FeS<sub>2</sub>@C hybrids for superior sodium-, potassium- and aluminum-ion storage, Energy Storage Mater 22 (2019) 228–234.

- [16] Q. Zhang, J. Mao, W.K. Pang, T. Zheng, V. Sencadas, Y. Chen, Y. Liu, Z. Guo, Boosting the potassium storage performance of alloy-based anode materials via electrolyte salt chemistry, Adv. Energy Mater. 8 (2018), 1703288.
- [17] Z. Yu, Y. Xie, B. Xie, C. Cao, Z. Zhang, H. Huo, Z. Jiang, Q. Pan, G. Yin, J. Wang, Uncovering the underlying science behind dimensionality in the potassium battery regime, Energy Storage Mater (2019), https://doi.org/10.1016/ i.ensm.2019.09.039.
- [18] J. Zheng, Y. Yang, X. Fan, G. Ji, X. Ji, H. Wang, S. Hou, M.R. Zachariah, C. Wang, Extremely stable antimony–carbon composite anodes for potassium-ion batteries, Energy Environ. Sci. 12 (2019) 615–623.
- [19] A.P. Cohn, N. Muralidharan, R. Carter, K. Share, L. Oakes, C.L. Pint, Durable potassium ion battery electrodes from high-rate cointercalation into graphitic carbons, J. Mater. Chem. 4 (2016) 14954–14959.
- [20] Y. Li, R.A. Adams, A. Arora, V.G. Pol, A.M. Levine, R.J. Lee, K. Akato, A.K. Naskar, M.P. Paranthaman, Sustainable potassium-ion battery anodes derived from wastetire rubber, J. Electrochem. Soc. 164 (2017) A1234–A1238.
- [21] C. Bommier, D. Mitlin, X. Ji, Internal structure-Na storage mechanisms-Electrochemical performance relations in carbons, Prog. Mater. Sci. 97 (2018) 170–203
- [22] Z. Xu, M. Wu, Z. Chen, C. Chen, J. Yang, T. Feng, E. Paek, D. Mitlin, Direct structure-performance comparison of all-carbon potassium and sodium ion capacitors, Adv. Sci. 6 (2019), 1802272.
- [23] S. Komaba, T. Hasegawa, M. Dahbi, K. Kubota, Potassium intercalation into graphite to realize high-voltage/high-power potassium-ion batteries and potassium-ion capacitors, Electrochem. Commun. 60 (2015) 172–175.
- [24] Z. Jian, S. Hwang, Z. Li, A.S. Hernandez, X. Wang, Z. Xing, D. Su, X. Ji, Hard-soft composite carbon as a long-cycling and high-rate anode for potassium-ion batteries, Adv. Funct. Mater. 27 (2017), 1700324.
- [25] L. Liu, Z. Lin, J.-Y. Chane-Ching, H. Shao, P.-L. Taberna, P. Simon, 3D rGO aerogel with superior electrochemical performance for K-ion battery, Energy Storage Mater 19 (2019) 306–313.
- [26] Y. Wang, Z. Wang, Y. Chen, H. Zhang, M. Yousaf, H. Wu, M. Zou, A. Cao, R.P.S. Han, Hyperporous sponge interconnected by hierarchical carbon nanotubes as a high-performance potassium-ion battery anode, Adv. Mater. 30 (2018), 1802074.
- [27] Z. Jian, W. Luo, X. Ji, Carbon electrodes for K-ion batteries, J. Am. Chem. Soc. 137 (2015) 11566–11569.
- [28] R.A. Adams, A. Varma, V.G. Pol, Temperature dependent electrochemical performance of graphite anodes for K-ion and Li-ion batteries, J. Power Sources 410–411 (2019) 124–131.
- [29] W. Zhang, Z. Wu, J. Zhang, G. Liu, N.-H. Yang, R.-S. Liu, W.K. Pang, W. Li, Z. Guo, Unraveling the effect of salt chemistry on long-durability high-phosphorusconcentration anode for potassium ion batteries, Nano Energy 53 (2018) 967–974.
- [30] Z. Chen, D. Yin, M. Zhang, Sandwich-like MoS<sub>2</sub>@SnO<sub>2</sub>@C with high capacity and stability for sodium/potassium ion batteries, Small 14 (2018), 1703818.
- [31] Y.-H. Zhu, Q. Zhang, X. Yang, E.-Y. Zhao, T. Sun, X.-B. Zhang, S. Wang, X.-Q. Yu, J.-M. Yan, Q. Jiang, Reconstructed orthorhombic V<sub>2</sub>O<sub>5</sub> polyhedra for fast ion diffusion in K-ion batteries, Inside Chem. 5 (2019) 168–179.
- [32] K. Cao, H. Liu, W. Li, Q. Han, Z. Zhang, K. Huang, Q. Jing, L. Jiao, CuO nanoplates for high-performance potassium-ion batteries, Small 159 (2019), 1901775.
- [33] L. Fang, J. Xu, S. Sun, B. Lin, Q. Guo, D. Luo, H. Xia, Few-layered Tin sulfide nanosheets supported on reduced graphene oxide as a high-performance anode for potassium-ion batteries, Small 15 (2019), 1804806.
- [34] C. Chen, Y. Yang, X. Tang, R. Qiu, S. Wang, G. Cao, M. Zhang, Graphene-encapsulated FeS<sub>2</sub> in carbon fibers as high reversible anodes for Na<sup>+</sup>/K<sup>+</sup> batteries in a wide temperature range, Small 15 (2019), 1804740.
- [35] D. Li, Y. Zhang, Q. Sun, S. Zhang, Z. Wang, Z. Liang, P. Si, L. Ci, Hierarchically porous carbon supported Sn<sub>4</sub>P<sub>3</sub> as a superior anode material or potassium-ion batteries, Energy Storage Mater (2019), https://doi.org/10.1016/ i.ensm.2019.04.037.
- [36] Y. Wang, Z. Zhang, G. Wang, X. Yang, Y. Sui, F. Du, B. Zou, Ultrafine Co<sub>2</sub>P nanorods wrapped by graphene enable a long cycle life performance for a hybrid potassium-ion capacitor, Nanoscale Horiz (2019), https://doi.org/10.1039/C9NH00211A.
- [37] Y. He, L. Wang, C. Dong, C. Li, X. Ding, Y. Qian, L. Xu, In-situ rooting ZnSe/N-doped hollow carbon architectures as high-rate and long-life anode materials for half/full sodium-ion and potassium-ion batteries, Energy Storage Mater (2019), https://doi.org/10.1016/j.ensm.2019.05.039.
- [38] H. Yu, X. Cheng, M. Xia, T. Liu, W. Ye, R. Zheng, N. Long, M. Shui, J. Shu, Pretreated commercial TiSe<sub>2</sub> as an insertion-type potassium container for constructing "Rocking-Chair" type potassium ion batteries, Energy Storage Mater 22 (2019) 154–159.
- [39] M. Naguib, R.A. Adams, Y. Zhao, D. Zemlyanov, A. Varma, J. Nanda, V.G. Pol, Electrochemical performance of MXenes as K-ion battery anodes, Chem. Commun. 53 (2017) 6883–6886.
- [40] Y. Liang, C. Luo, F. Wang, S. Hou, S.-C. Liou, T. Qing, Q. Li, J. Zheng, C. Cui, C. Wang, An organic anode for high temperature potassium-ion batteries, Adv. Energy Mater. 9 (2019), 1802986.
- [41] K. Lei, F. Li, C. Mua, J. Wang, Q. Zhao, C. Chen, J. Chen, High K-storage performance based on the synergy of dipotassium terephthalate and ether-based electrolyte, Energy Environ. Sci. 10 (2017) 552–557.
- [42] X. Wu, Y. Chen, Z. Xing, C.W.K. Lam, S.S. Pang, W. Zhang, Z. Ju, Advanced carbon-based anodes for potassium-ion batteries, Adv. Energy Mater. 9 (2019), 1900343.
- [43] R. Raccichini, A. Varzi, S. Passerini, B. Scrosati, The role of graphene for electrochemical energy storage, Nat. Mater. 14 (2015) 271–279.

- [44] X. Qi, K. Huang, X. Wu, W. Zhao, H. Wang, Q. Zhuang, Z. Ju, Novel fabrication of N-doped hierarchically porous carbon with exceptional potassium storage properties, Carbon 131 (2018) 79–85.
- [45] M. Chen, W. Wang, X. Liang, S. Gong, J. Liu, Q. Wang, S. Guo, H. Yang, Sulfur/oxygen codoped porous hard carbon microspheres for high-performance potassium-ion batteries, Adv. Energy Mater. 8 (2018), 1800171.
- [46] Z. Jian, Z. Xing, C. Bommier, Z. Li, X. Ji, Hard carbon microspheres: potassium-ion anode versus sodium-ion anode, Adv. Energy Mater. 6 (2016), 1501874.
- [47] Y. Xu, C. Zhang, M. Zhou, Q. Fu, C. Zhao, M. Wu, Y. Lei, Highly nitrogen doped carbon nanofibers with superior rate capability and cyclability for potassium ion batteries, Nat. Commun. 9 (2018) 1720.
- [48] Y. Qian, S. Jiang, Y. Li, Z. Yi, J. Zhou, T. Li, Y. Han, Y. Wang, J. Tian, N. Lin, Y. Qian, In situ revealing the electroactivity of P-O and P-C bonds in hard carbon for high-capacity and long-life Li/K-ion batteries, Adv. Energy Mater. 9 (2019), 1901676
- [49] J. Ruan, Y. Zhao, S. Luo, T. Yuan, J. Yang, D. Sun, S. Zheng, Fast and stable potassium-ion storage achieved by in situ molecular self-assembling N/O dualdoped carbon network, Energy Storage Mater (2019), https://doi.org/10.1016/ i.ensm.2019.05.037.
- [50] W. Qiu, H. Xiao, Y. Li, X. Lu, Y. Tong, Nitrogen and phosphorus codoped vertical graphene/carbon cloth as a binder-free anode for flexible advanced potassium ion full batteries, Small 15 (2019), 1901285.
- [51] K. Share, A.P. Cohn, R. Carter, B. Rogers, C.L. Pint, Role of nitrogen-doped graphene for improved high-capacity potassium ion battery anodes, ACS Nano 10 (2016) 9738–9744.
- [52] N. Chen, X. Huang, L. Qu, Heteroatom substituted and decorated graphene: preparation and applications, Phys. Chem. Chem. Phys. 17 (2015) 32077–32098.
- [53] V.H. Pham, J.A. Boscoboinik, D.J. Stacchiola, E.C. Self, P. Manikandan, S. Nagarajan, Y. Wang, V.G. Pol, J. Nanda, E. Paek, D. Mitlin, Selenium-sulfur (SeS) fast charging cathode for sodium and lithium metal batteries, Energy Storage Mater 20 (2019) 71–79.
- [54] W. Ai, Z. Luo, J. Jiang, J. Zhu, Z. Du, Z. Fan, L. Xie, H. Zhang, W. Huang, T. Yu, Nitrogen and sulfur codoped graphene: multifunctional electrode materials for high-performance Li-ion batteries and oxygen reduction reaction, Adv. Mater. 26 (2014) 6186–6192.
- [55] X. Miao, D. Sun, X. Zhou, Z. Lei, Designed formation of nitrogen and sulfur dual-doped hierarchically porous carbon for long-life lithium and sodium ion batteries, Chem. Eng. J. 364 (2019) 208–216.
- [56] G. Zou, H. Hou, C.W. Foster, C.E. Banks, T. Guo, Y. Jiang, Y. Zhang, X. Ji, Advanced hierarchical vesicular carbon co-doped with S, P, N for high-rate sodium sorage, Adv. Sci. 5 (2018), 1800241.
- [57] T. Liu, Y. Zhang, Z. Jiang, X. Zeng, J. Ji, Z. Li, X. Gao, M. Sun, Z. Lin, M. Ling, J. Zheng, C. Liang, Exploring competitive features of stationary sodium ion batteries for electrochemical energy storage, Energy Environ. Sci. 12 (2019) 1512–1533.
- [58] J. Chen, B. Yang, H. Li, P. Ma, J. Lang, X. Yan, Candle Soot: onion-like carbon, an advanced anode material for potassium-ion hybrid capacitor, J. Mater. Chem. 7 (2019) 9247.
- [59] J. Chen, B. Yang, H. Hou, H. Li, L. Liu, L. Zhang, X. Yan, Disordered, large interlayer spacing, and oxygen-rich carbon nanosheets for potassium ion hybrid capacitor, Adv. Energy Mater. 9 (2019), 1803894.
- [60] G. Lu, H. Wang, Y. Zheng, H. Zhang, Y. Yang, J. Shi, M. Huang, W. Liu, Metalorganic framework derived N-doped CNT@porous carbon for high-performance sodium- and potassium-ion storage, Electrochim. Acta 319 (2019) 541–551.
- [61] J.P. Paraknowitsch, A. Thomas, Doping carbons beyond nitrogen: an overview of advanced heteroatom doped carbons with boron, sulphur and phosphorus for energy applications, Energy Environ. Sci. 6 (2013) 2839–2855.
- [62] L. Wu, D. Buchholz, C. Vaalma, G.A. Giffin, S. Passerini, Apple-biowaste-derived hard carbon as a powerful anode material for Na-ion batteries, ChemElectroChem 3 (2016) 292–298.
- [63] J. Li, W. Qin, J. Xie, H. Lei, Y. Zhu, W. Huang, X. Xu, Z. Zhao, W. Mai, Sulphur-doped reduced graphene oxide sponges as high-performance freestanding anodes for K-ion storage, Nano Energy 53 (2018) 415–424.
- [64] J. Ding, H. Zhang, H. Zhou, J. Feng, X. Zheng, C. Zhong, E. Paek, W. Hu, D. Mitlin, Sulfur-grafted hollow carbon spheres for potassium-ion battery anodes, Adv. Mater. 31 (2019), 1900429.
- [65] C. Lv, W. Xu, H. Liu, L. Zhang, S. Chen, X. Yang, X. Xu, D. Yang, 3D sulfur and nitrogen codoped carbon nanofiber aerogels with optimized electronic structure and enlarged interlayer spacing boost potassium-ion storage, Small 15 (2019), 1900816.
- [66] J. Yang, Z. Ju, Y. Jiang, Z. Xing, B. Xi, J. Feng, S. Xiong, Enhanced capacity and rate capability of nitrogen/oxygen dual-doped hard carbon in capacitive potassium-ion storage, Adv. Mater. 30 (2018), 1700104.
- [67] H. He, D. Huang, Y. Tang, Q. Wang, X. Ji, H. Wang, Z. Guo, Tuning nitrogen species in three-dimensional porous carbon via phosphorus doping for ultra-fast potassium storage, Nano Energy 57 (2019) 728–736.
- [68] J. Bai, B. Xi, H. Mao, Y. Lin, X. Ma, J. Feng, S. Xiong, One-step construction of N,P-codoped porous carbon sheets/CoP hybrids with enhanced lithium and potassium storage, Adv. Mater. 30 (2018), 1802310.
- [69] W. Li, M. Zhou, H. Li, K. Wang, S. Cheng, K. Jiang, A high performance sulfur-doped disordered carbon anode for sodium ion batteries, Energy Environ. Sci. 8 (2015) 2916–2921.
- [70] D. Xu, C. Chen, J. Xie, B. Zhang, L. Miao, J. Cai, Y. Huang, L. Zhang, A hierarchical N/S-codoped carbon anode fabricated facilely from cellulose/polyaniline microspheres for high-performance sodium-ion batteries, Adv. Energy Mater. 6 (2016), 1501929.

- [71] J. Ruan, T. Yuan, Y. Pang, S. Luo, C. Peng, J. Yang, S. Zheng, Nitrogen and sulfur dual-doped carbon films as flexible free-standing anodes for Li-ion and Na-ion batteries, Carbon 126 (2018) 9–16.
- [72] J. Liang, Y. Jiao, M. Jaroniec, S.Z. Qiao, Sulfur and nitrogen dual-doped mesoporous graphene electrocatalyst for oxygen reduction with synergistically enhanced performance, Angew. Chem. Int. Ed. 51 (2012) 11496–11500.
- [73] Y. Liu, H. Dai, L. Wu, W. Zhou, L. He, W. Wang, W. Yan, Q. Huang, L. Fu, Y. Wu, A large scalable and low-cost sulfur/nitrogen dual-doped hard carbon as the negative electrode material for high-performance potassium-ion batteries, Adv. Energy Mater. 9 (2019), 1901379.
- [74] D. Puthusseri, V. Aravindan, S. Madhavi, S. Ogale, 3D micro-porous conducting carbon beehive by single step polymer carbonization for high performance supercapacitors: the magic of in situ porogen formation, Energy Environ. Sci. 7 (2014) 728–735.
- [75] H.H. Wei, Q. Zhang, Y. Wang, Y.J. Li, J.C. Fan, Q.J. Xu, Y.L. Min, Baby diaperinspired construction of 3D porous composites for long-term lithium-ion batteries, Adv. Funct. Mater. 28 (2018), 1704440.
- [76] Z. Yuan, L. Si, X. Zhu, Three-dimensional hard carbon matrix for sodiumion battery anode with superior-rate performance and ultralong cycle life, J. Mater. Chem. 3 (2015) 23403–23411.
- [77] H. Wang, Y. Yang, Y. Liang, J.T. Robinson, Y. Li, A. Jackson, Y. Cui, H. Dai, Graphene-wrapped sulfur particles as a rechargeable lithium sulfur battery cathode material with high capacity and cycling stability, Nano Lett. 11 (2011) 2644–2647
- [78] S. Wei, L. Ma, K.E. Hendrickson, Z. Tu, L.A. Archer, Metal-sulfur battery cathodes based on PAN-sulfur composites, J. Am. Chem. Soc. 137 (2015) 12143–12152.
- [79] X. Yang, L. Zhang, F. Zhang, Y. Huang, Y. Chen, Sulfur-infiltrated graphene-based layered porous carbon cathodes for high-performance lithium-sulfur batteries, ACS Nano 8 (2014) 5208–5215.
- [80] C. Zhang, H. Bin Wu, C. Yuan, Z. Guo, X.W. Lou, Angew. Chem. Int. Ed. 51 (2012) 9592–9595
- [81] J. Pokrzywinski, J.K. Keum, R.E. Ruther, E.C. Self, M. Chi, H. Meyer Iii, K.C. Littrell, D. Aulakh, S. Marble, J. Ding, M. Wriedt, J. Nanda, D. Mitlin, Unrivaled combination of surface area and pore volume in micelle-templated carbon for supercapacitor energy storage, J. Mater. Chem. 5 (2017) 13511–13525.
- [82] C. Ma, W. Zhang, Y.S. He, Q. Gong, H. Che, Z.F. Ma, Carbon coated SnO<sub>2</sub> nanoparticles anchored on CNT as a superior anode material for lithium-ion batteries, Nanoscale 8 (2016) 4121–4126.
- [83] M. Sevilla, A.B. Fuertes, Direct synthesis of highly porous interconnected carbon nanosheets and their application as high performance supercapacitors, ACS Nano 8 (2014) 5069–5078.
- [84] C. Gao, Q. Wang, S. Luo, Z. Wang, Y. Zhang, Y. Liu, A. Hao, R. Guo, High performance potassium-ion battery anode based on biomorphic N-doped carbon derived from walnut septum, J. Power Sources 415 (2019) 165–171.
- [85] R. Huang, M. Huang, X. Li, F. An, N. Koratkar, Z.Z. Yu, Porous graphene films with unprecedented elastomeric scaffold-like folding behavior for foldable energy storage devices. Adv. Mater. 30 (2018), 1707025.
- [86] T. Wu, M. Jing, L. Yang, G. Zou, H. Hou, Y. Zhang, Y. Zhang, X. Cao, X. Ji, Controllable chain-length for covalent sulfur-carbon materials enabling stable and high-capacity sodium storage, Adv. Energy Mater. 9 (2019), 1803478.
- [87] X. Wang, Y. Qian, L. Wang, H. Yang, H. Li, Y. Zhao, T. Liu, Sulfurized polyacrylonitrile cathodes with high compatibility in both ether and carbonate electrolytes for ultrastable lithium-sulfur batteries, Adv. Funct. Mater. (2019), 1902929.
- [88] B. Sainbileg, Y.-B. Lan, J.-K. Wang, M. Hayashi, Deciphering anomalous Raman features of regioregular poly (3-hexylthiophene) in ordered aggregation form, J. Phys. Chem. C 122 (2018) 4224–4231.
- [89] Z. Hong, Y. Zhen, Y. Ruan, M. Kang, K. Zhou, J.M. Zhang, Z. Huang, M. Wei, Rational design and general synthesis of S-doped hard carbon with tunable doping sites toward excellent Na-ion storage performance, Adv. Mater. 30 (2018), 1802035.
- [90] J. Huang, X. Guo, X. Du, X. Lin, J.Q. Huang, H. Tan, Y. Zhu, B. Zhang, Nanostructures of solid electrolyte interphases and their consequences for microsized Sn anodes in sodium ion batteries, Energy Environ. Sci. 12 (2019) 1550–1557.
- [91] Y. Li, K. Yan, H.-W. Lee, Z. Lu, N. Liu, Y. Cui, Growth of conformal graphene cages on micrometre-sized silicon particles as stable battery anodes, Nat. Energy 1 (2016) 15029.
- [92] J. Ding, H. Wang, Z. Li, K. Cui, D. Karpuzov, X. Tan, A. Kohandehghan, D. Mitlin, Peanut shell hybrid sodium ion capacitor with extreme energy-power rivals lithium ion capacitors, Energy Environ. Sci. 8 (2015) 941–955.
- [93] G. Zou, H. Hou, G. Zhao, Z. Huang, P. Ge, X. Ji, Preparation of S/N-codoped carbon nanosheets with tunable interlayer distance for high-rate sodium-ion batteries, Green Chem. 19 (2017) 4622–4632.
- [94] L. Fan, R. Ma, Y. Yang, S. Chen, B. Lu, Covalent sulfur for advanced room temperature sodium-sulfur batteries, Nano Energy 28 (2016) 304–310.
- [95] J. Ye, H. Zhao, W. Song, N. Wang, M. Kang, Z. Li, Enhanced electronic conductivity and sodium-ion adsorption in N/S codoped ordered mesoporous carbon for high-performance sodium-ion battery anode, J. Power Sources 412 (2019) 606–614.
- [96] J. Qian, F. Wu, Y. Ye, M. Zhang, Y. Huang, Y. Xing, W. Qu, L. Li, R. Chen, Boosting fast sodium storage of a large-scalable carbon anode with an ultralong cycle life, Adv. Energy Mater. 8 (2018), 1703159.
- [97] X. Chang, Y. Ma, M. Yang, T. Xing, L. Tang, T. Chen, Q. Guo, X. Zhu, J. Liu, H. Xia, In-situ solid-state growth of N, S codoped carbon nanotubes encapsulating metal

- sulfides for high-efficient-stable sodium ion storage, Energy Storage Mater (2019), https://doi.org/10.1016/j.ensm.2019.04.039.
- [98] H. Liu, X. Liu, H. Wang, Y. Zheng, H. Zhang, J. Shi, W. Liu, M. Huang, J. Kan, X. Zhao, D. Li, High-performance sodium-ion capacitor constructed by wellmatched dual-carbon electrodes from a single biomass, ACS Sustain. Chem. Eng. 7 (2019) 12188–12199.
- [99] W. Zhang, J. Ming, W. Zhao, X. Dong, M.N. Hedhili, P.M.F.J. Costa, H.N. Alshareef, Graphitic nanocarbon with engineered defects for highperformance potassium-ion battery anodes, Adv. Funct. Mater. 29 (2019), 1903641.
- [100] Y. Qiao, M. Ma, Y. Liu, S. Li, Z. Lu, H. Yue, H. Dong, Z. Cao, Y. Yin, S. Yang, First-principles and experimental study of nitrogen/sulfur co-doped carbon nanosheets as anodes for rechargeable sodium ion batteries, J. Mater. Chem. 4 (2016) 15565–15574.
- [101] C. Xu, Q. Han, Y. Zhao, L. Wang, Y. Li, L. Qu, Sulfur-doped graphitic carbon nitride decorated with graphene quantum dots for an efficient metal-free electrocatalyst, J. Mater. Chem. 3 (2015) 1841–1846.
- [102] X. Ma, X. Song, Z. Yu, S. Li, X. Wang, L. Zhao, L. Zhao, Z. Xiao, C. Qi, G. Ning, J. Gao, S doping coupled with pore-structure modulation to the conductive carbon black: toward high mass loading electrical double-layer capacitor, Carbon 149 (2019) 646–654.
- [103] H. Wang, Z. Xu, A. Kohandehghan, Z. Li, K. Cui, X. Tan, T.J. Stephenson, C.K. King'ondu, C.M.B. Holt, B.C. Olsen, J.K. Tak, D. Harfield, A.O. Anyia, D. Mitlin, Interconnected carbon nanosheets derived from Hemp for ultrafast supercapacitors with high energy, ACS Nano 7 (2013) 5131–5141.
- [104] R. Hao, H. Lan, C. Kuang, H. Wang, L. Guo, Superior potassium storage in chitinderived natural nitrogen-doped carbon nanofibers, Carbon 128 (2018) 224–230.
- [105] E. Memarzadeh Lotfabad, P. Kalisvaart, A. Kohandehghan, D. Karpuzov, D. Mitlin, Origin of non-SEI related coulombic efficiency loss in carbons tested against Na and Li, J. Mater. Chem. 2 (2014) 19685–19695.
- [106] X. Hu, Y. Liu, J. Chen, L. Yi, H. Zhan, Z. Wen, Fast redox kinetics in Bi-heteroatom doped 3D porous carbon nanosheets for high-performance hybrid potassium-ion battery capacitors, Adv. Energy Mater. 9 (2019), 1901533.
- [107] W. Yang, J. Zhou, S. Wang, W. Zhang, Z. Wang, F. Lv, K. Wang, Q. Sun, S. Guo, Freestanding film made by necklace-like N-doped hollow carbon with hierarchical pores for high-performance potassium-ion storage, Energy Environ. Sci. 12 (2019) 1605–1612.
- [108] H. Tang, D. Yan, T. Lu, L. Pan, Sulfur-doped carbon spheres with hierarchical micro/mesopores as anode materials for sodium-ion batteries, Electrochim. Acta 241 (2017) 63–72.
- [109] G. Ning, X. Ma, X. Zhu, Y. Cao, Y. Sun, C. Qi, Z. Fan, Y. Li, X. Zhang, X. Lan, J. Gao, Enhancing the Li storage capacity and initial coulombic efficiency for porous carbons by sulfur doping, ACS Appl. Mater. Interfaces 6 (2014) 15950–15958.
- [110] R.A. Adams, J.M. Syu, Y. Zhao, C.T. Lo, A. Varma, V.G. Pol, Binder-free N- and O-rich carbon nanofiber anodes for long cycle life K-ion batteries, ACS Appl. Mater. Interfaces 9 (2017) 17872–17881.
- [111] B. Yang, J. Chen, L. Liu, P. Ma, B. Liu, J. Lang, Y. Tang, X. Yan, 3D nitrogen-doped framework carbon for high-performance potassium ion hybrid capacitor, Energy Storage Mater (2019). https://doi.org/10.1016/j.ensm.2019.04.008
- Storage Mater (2019), https://doi.org/10.1016/j.ensm.2019.04.008.
  [112] A. Mahmood, S. Li, Z. Ali, H. Tabassum, B. Zhu, Z. Liang, W. Meng, W. Aftab, W. Guo, H. Zhang, M. Yousaf, S. Gao, R. Zou, Y. Zhao, Ultrafast sodium/potassiumion intercalation into hierarchically porous thin carbon shells, Adv. Mater. 31 (2019), 1805430.
- [113] X. Zhao, Y. Tang, C. Ni, J. Wang, A. Star, Y. Xu, Free-standing nitrogen-doped cupstacked carbon nanotube mats for potassium-ion battery anodes, ACS Appl. Energy Mater. 1 (2018) 1703–1707.
- [114] D. Liu, X. Huang, D. Qu, D. Zheng, G. Wang, J. Harris, J. Si, T. Ding, J. Chen, D. Qu, Confined phosphorus in carbon nanotube-backboned mesoporous carbon as superior anode material for sodium/potassium-ion batteries, Nano Energy 52 (2018) 1–10.
- [115] Z. Ju, P. Li, G. Ma, Z. Xing, Q. Zhuang, Y. Qian, Few layer nitrogen-doped graphene with highly reversible potassium storage, Energy Storage Mater 11 (2018) 38–46.
- [116] Y. Li, W. Zhong, C. Yang, F. Zheng, Q. Pan, Y. Liu, G. Wang, X. Xiong, M. Liu, N/S codoped carbon microboxes with expanded interlayer distance toward excellent potassium storage, Chem. Eng. J. 358 (2019) 1147–1154.
- [117] J.-Y. Hwang, H.M. Kim, C.S. Yoon, Y.-K. Sun, Toward high-safety potassium-sulfur batteries using a potassium polysulfide catholyte and metal-free anode, ACS Energy Lett 3 (2018) 540–541.
- [118] S. Gu, N. Xiao, F. Wu, Y. Bai, C. Wu, Y. Wu, Chemical synthesis of K<sub>2</sub>S<sub>2</sub> and K<sub>2</sub>S<sub>3</sub> for probing electrochemical mechanisms in K-S Batteries, ACS Energy Lett 3 (2018) 2858–2864.
- [119] Y. Lei, D. Han, J. Dong, L. Qin, X. Li, D. Zhai, B. Li, Y. Wu, F. Kang, Unveiling the influence of electrode/electrolyte interface on the capacity fading for typical graphite-based potassium-ion batteries, Energy Storage Mater 24 (2020) 319–328.
- [120] L. Qin, N. Xiao, J. Zheng, Y. Lei, D. Zhai, Y. Wu, Localized high-concentration electrolytes boost potassium storage in high-loading graphite, Adv. Energy Mater. 9 (2019), 1902618.
- [121] J. Kan, H. Wang, H. Zhang, J. Shi, W. Liu, D. Li, G. Dong, Y. Yang, R. Gao, Nitrogen functionalized carbon nanocages optimized as high-performance anodes for sodium ion storage, Electrochim. Acta 304 (2019) 192–201.
- [122] Z. Zhang, M. Li, Y. Gao, Z. Wei, M. Zhang, C. Wang, Y. Zeng, B. Zou, G. Chen, F. Du, Fast potassium storage in hierarchical Ca<sub>0.5</sub>Ti<sub>2</sub>(PO<sub>4</sub>)<sub>3</sub>@C microspheres enabling high-performance potassium-ion capacitors, Adv. Funct. Mater. 28 (2018), 1802684.

- [123] L. Fan, K. Lin, J. Wang, R. Ma, B. Lu, A nonaqueous potassium-based batterysupercapacitor hybrid device, Adv. Mater. 30 (2018), 1800804.
- [124] S. Dong, Z. Li, Z. Xing, X. Wu, X. Ji, X. Zhang, Novel potassium-ion hybrid capacitor based on an anode of  $K_2Ti_6O_{13}$  microscaffolds, ACS Appl. Mater. Interfaces 10 (2018) 15542–15547.
- [125] A.L. Comte, Y. Reynier, C. Vincens, C. Leys, P. Azaïs, First prototypes of hybrid potassium-ion capacitor (KIC): an innovative, cost-effective energy storage technology for transportation applications, J. Power Sources 363 (2017) 34–43.
- [126] X. Yang, A.L. Rogach, Electrochemical techniques in battery research: a tutorial for nonelectrochemists, Adv. Energy Mater. 9 (2019), 1900747.
- [127] W. Wang, J. Zhou, Z. Wang, L. Zhao, P. Li, Y. Yang, C. Yang, H. Huang, S. Guo, Short-range order in mesoporous carbon boosts potassium-ion battery performance, Adv. Energy Mater. 8 (2018), 1701648.
- [128] X. Cheng, H. Zhu, H. Yu, W. Ye, R. Zheng, T. Liu, N. Peng, M. Shui, J. Shu, K<sub>2</sub>Nb<sub>8</sub>O<sub>21</sub> nanotubes with superior electrochemical performance for ultrastable lithium storage, J. Mater. Chem. 6 (2018) 8620–8632.
- [129] Q. Pang, D. Kundu, M. Cuisinier, L.F. Nazar, Surface-enhanced redox chemistry of polysulphides on a metallic and polar host for lithium-sulphur batteries, Nat. Commun. 5 (2014) 4759.
- [130] F.J. Sonia, M.K. Jangid, M. Aslam, P. Johari, A. Mukhopadhyay, Enhanced and faster potassium storage in graphene with respect to graphite: a comparative study with lithium storage, ACS Nano 13 (2019) 2190–2204.
- [131] J.W. Christian, The Theory of Transformations in Metals and Alloys, vol. I, Pergamon Press, Oxford, 1975.
- [132] J. Zhao, X. Zou, Y. Zhu, Y. Xu, C. Wang, Electrochemical intercalation of potassium into graphite, Adv. Funct. Mater. 26 (2016) 8103–8110.
- [133] L. Fan, Q. Liu, S. Chen, K. Lin, Z. Xu, B. Lu, Potassium-based dual ion battery with dual-graphite electrode, Small 13 (2017), 1701011.

- [134] A. Noori, M.F. El-Kady, M.S. Rahmanifar, R.B. Kaner, M.F. Mousavi, Towards establishing standard performance metrics for batteries, supercapacitors and beyond, Chem. Soc. Rev. 48 (2019) 1272–1341.
- [135] a) A.J. Bard, L.R. Faulkner, Fundamentals and Applications, Wiley, New York, 1980;
  - b) N. Perez, Electrochemistry and Corrosion Science, Kluwer Academic Publishers, 2004;
  - c) V.S. Bagotsky, Fundamentals of Electrochemistry, second ed., The Electrochemical Society, Penningt, NJ, 2006.
- [136] D. Qiu, J. Guan, M. Li, C. Kang, J. Wei, Y. Li, Z. Xie, F. Wang, R. Yang, Kinetics enhanced nitrogen-doped hierarchical porous hollow carbon spheres boosting advanced potassium-ion hybrid capacitors, Adv. Funct. Mater. 29 (2019), 1903496.
- [137] K. Tang, X. Yu, J. Sun, H. Li, X. Huang, Kinetic analysis on LiFePO<sub>4</sub> thin films by CV, GITT, and EIS, Electrochim. Acta 56 (2011) 4869–4875.
- [138] V.L. Tauson, A.N. Sapozhnikov, S.N. Shinkareva, E.E. Lustenberg, The nature of the stability of an incommensurate 3D structural modulation in baikal lazurite: experimental data at 550°C, Geochem. Int. 47 (2009) 815–830.
- [139] R. Ma, L. Fan, J. Wang, B. Lu, Confined and covalent sulfur for stable room temperature potassium sulfur battery, Electrochim. Acta 293 (2019) 191–198.
- [140] P. Xiong, X. Han, X. Zhao, P. Bai, Y. Liu, J. Sun, Y. Xu, Room-temperature potassium-sulfur batteries enabled by microporous carbon stabilized smallmolecule sulfur cathodes, ACS Nano 13 (2019) 2536–2543.
- [141] S. Liu, J. Zhou, H. Song, Tailoring highly N-doped carbon materials from hexamine-based MOFs: superior performance and new insight into the roles of N configurations in Na-ion storage, Small 14 (2018), 1703548.